THE ASTROPHYSICAL JOURNAL, 431:201–222, 1994 August 10

GAS KINEMATICS AND IONIZATION ALONG THE EXTENDED SIGHT LINE TO HD 116852[1]

KENNETH R. SEMBACH[2] AND BLAIR D. SAVAGE[3]

Received 1993 November 15; accepted 1994 February 9

ABSTRACT

We present Goddard High-Resolution Spectrograph intermediate observations of the interstellar medium toward HD 116852, a low halo star at a distance of 4.8 kpc ($z = -1.3$ kpc) in the direction $l = 304\overset{\circ}{.}9$, $b = 16\overset{\circ}{.}1$. The small science aperture observations have signal-to-noise ratios ranging from 30 to 90 and resolutions of 11 to 18 km s^{-1} (FWHM). We confirm the optical MK classification of this star through an analysis of its ultraviolet photospheric and stellar wind profiles. We detect interstellar lines of Al III, Si IV, C IV, and N V together with lines of C I, C I*, C I**, Si II, Ge II, P II, and Ni II. We convert the Mg II, P II, S II, Al III, Si IV, C IV, and N V profiles into measures of apparent column density as a function of LSR velocity. Gas scale height, velocity dispersion, and differential Galactic rotation effects govern the profile shapes. A simple computer model of the expected sight line column density profiles for the low and high ion species indicates that the gas velocity dispersions and scale heights increase as the ionization level of the gas increases. We find scale heights $H \geq 1$ kpc for the high ions, which are comparable to the z-distance of the star, whereas we find $H \approx 0.6$ to 0.7 kpc for Al III and $H \approx 0.1$ kpc for P II and Ge II. An enhancement in the Al II profile near -15 km s^{-1} accounts for approximately 25% of the Al III column along the sight line and probably arises within gas located approximately 500 pc below the Sagittarius-Carina spiral arm link. Portions of the broad underlying Al III distribution are associated with the higher ionization lines, perhaps in conductive interfaces. The presence of N V and the column density ratios of Si IV, C IV, and N V favor the interpretation that much of the high ion absorption is produced by collisional ionization in gas with $T = 1\text{–}3 \times 10^5$ K. An enhancement near -35 km s^{-1} in both the Si IV and C IV profiles may be due to an outflow from the Norma spiral arm at a z-distance of about -1 kpc. The smooth decrease of the N(C IV)/N(Si IV) ratio at negative velocities may be due to an ISM ionization structure for hot gas that changes with distance from the Galactic plane or to a two phase gas distribution in which the relative contribution from each phase changes with distance from the Galactic plane.

Subject headings: Galaxy: halo — ISM: abundances — stars: individual (HD 116852)

1. INTRODUCTION

Our understanding of the physical state, kinematics, and distribution of Milky Way halo gas is progressing rapidly as a result of spectroscopic investigations of distant O and B stars in the Galaxy. High-dispersion ($R \sim 12{,}000$) data from the *International Ultraviolet Explorer* (*IUE*) satellite show that highly ionized species, such as Si IV, C IV, and N V, are present in sufficient quantities within the ISM to be important diagnostics of gas that has been heated to $T \approx 10^6$ K by energetic events such as supernova explosions. Even though these species are not effective tracers of gas at $T \approx 10^6$ K, they are natural by-products of the hot, cooling gas. Reliable N V detections along several extended sight lines have provided compelling evidence that the high ion gas has temperatures near 2×10^5 K. *IUE* studies of the high ion profiles along many sight lines (Pettini & West 1982; Savage & Massa 1987; Sembach & Savage 1992) also indicate that substantial fractions of the Si IV, C IV, and N V absorption are created under similar conditions in a gas distribution that extends several kpc from the Galactic plane, although some differences in the kinematics and distributions of the three species exist.

The Goddard High-Resolution Spectrograph (GHRS) onboard the *Hubble Space Telescope* (*HST*) provides an unparalleled opportunity to study the high ions at resolutions and signal-to-noise ratios much higher than those afforded by the *IUE* spectrographs. Savage, Sembach, & Cardelli (1994) are using the GHRS in its highest resolution (FWHM = 3.5 km s^{-1}) mode to analyze the highly ionized gas absorption toward HD 167756 ($l = 351°$, $b = -12°$, $d = 4$ kpc, $z = -0.85$ kpc) and find evidence for two distinct types of high ion gas. Much of the Si IV and portions of the C IV are produced by collisional ionization at $T \approx 10^5$ K in conduction fronts. A hotter ($T \sim 2\text{–}8 \times 10^5$ K) gas type traced primarily by C IV and N V is also present. Hints of the complex character of gas along the HD 167756 sight line are present in high-quality *IUE* profiles (Sembach & Savage 1992), but it is only with the full resolving power and signal-to-noise capabilities available with the GHRS that the velocity structure in the profiles can be examined in sufficient detail to provide strong constraints on the physical conditions within the gas.

Other GHRS studies are providing new information about the kinematics and ionization of gas toward halo stars in the solar neighborhood. Spitzer & Fitzpatrick (1992) have used the GHRS echelle gratings to study the high ion absorption toward the distant high-latitude star HD 93521 ($l = 183°$,

---

[1] Based on observations obtained with the Goddard High-Resolution Spectrograph on the NASA/ESA *Hubble Space Telescope*, obtained at the Space Telescope Science Institute, which is operated by the Association of Universities for Research in Astronomy, Inc., under NASA contract NAS5-26555.

[2] Center for Space Research, 6-216, Massachusetts Institute of Technology, 77 Massachusetts Avenue, Cambridge, Massachusetts 02139; E-mail: sembach@sundoggie.mit.edu.

[3] Washburn Observatory, University of Wisconsin-Madison, 475 North Charter Street, Madison, Wisconsin 53706;
E-mail: savage@madraf.astro.wisc.edu.

$b = +62^\circ$, $d = 1.7$ kpc, $z = +1.5$ kpc) and found that the Si IV and C IV line velocities are shifted relative to one another as might be expected for cooling gas returning to the Galactic plane. GHRS observations toward the high-latitude stars HD 18100 ($l = 218^\circ$, $b = -63^\circ$, $d = 3.1$ kpc, $z = -2.8$ kpc) and HD 100340 ($l = 259^\circ$, $b = +61^\circ$, $d = 5.3$ kpc, $z = +4.6$ kpc) using the GHRS intermediate resolution gratings (FWHM = 11 to 18 km s^{-1}) also reveal the presence of multiple highly ionized gas clouds with outflowing and infalling motions (Savage & Sembach 1994). The HD 18100 and HD 100340 data clearly reveal distinct differences in the Si IV and N V absorption characteristics like those seen toward HD 167756.

In this paper, we extend our study of gas properties in the low Galactic halo to the HD 116852 sight line. HD 116852 is an O9 III halo star situated in the direction $l = 304^\circ.9$, $b = -16^\circ.1$ at a distance of 4.8 kpc and a Galactocentric radius of 7.0 kpc. The sight line penetrates through the Galactic disk and into the low halo out to a z-distance of -1.3 kpc. To a large extent, differential Galactic rotation governs the shapes of the HD 116852 absorption profiles and allows us to trace the absorption properties as a function of distance (velocity) along the sight line in more detail than has been possible for previous sight lines observed with the intermediate resolution gratings of the GHRS.

In § 2 we describe the observations and outline the data reduction procedures. Section 3 is an overview of the stellar and interstellar absorption observed toward HD 116852. We give a description of the sight line properties in § 4. Section 5 contains our data analysis methods and a discussion of the low, intermediate, and high ion apparent column density profiles. We present a kinematical analysis of the data set and a discussion of the gas ionization along the sight line in §§ 6 and 7. Section 8 is a summary of the primary results of the paper.

2. OBSERVATIONS AND REDUCTION

To learn about the ionization structure and kinematical character of gas in the Galactic halo, we acquired GHRS intermediate resolution (G160M) data for the Al III $\lambda\lambda$1854, 1862; Si IV $\lambda\lambda$1393, 1402; C IV $\lambda\lambda$1548, 1550; and N V $\lambda\lambda$1238, 1242 lines toward HD 116852 in 1992 November as part of *HST* program GTO 3960. A variety of low ionization lines are present in the high ion spectral integrations. We obtained additional observations of low ion lines in the 2050, 2260, and 2600 Å spectral regions with the intermediate or high-resolution gratings (G200M, G270M, Ech-B) in 1993 May, and these longer wavelength data will be analyzed in a forthcoming paper. Table 1 contains details of the wavelength coverage, nominal resolution, exposure time, and interstellar species present in the G160M observations studied in this paper. These observations are preserved in the *HST* data archive in the files listed in the first column of Table 1.

All data were acquired with the 500 diode photon counting digicon detector using the FP-Split and comb-addition procedures to reduce the detector fixed-pattern noise (see Duncan & Ebbets 1990). Scanning was performed with detector step pattern 6, which provides two samples per diode width and measurements of the detector background adjacent to the first order spectra. To preserve the resolution offered by G160M grating, only the small science aperture (SSA: $0''.25 \times 0''.25$) was used, thereby avoiding the broad instrumental spread function (ISF) wings resulting from the *HST* spherical aberration; the ISF for the SSA data analyzed in this study is reasonably approximated by a Gaussian function having a wavelength dependent width (see Table 1). For information about the spectrograph, gratings, apertures, and data acquisition procedures see Duncan (1992).

Spectral extraction, paired pulse corrections, background subtraction, and wavelength assignment for all spectra were carried out using standard GHRS data reduction routines available at the Space Telescope Science Institute and the University of Wisconsin-Madison as of 1993 April. The adopted background was an average of the levels measured with the full diode array to each side of the first-order spectrum as part of the scanning sequence. No additional scattered light corrections were necessary for the G160M data because such corrections for the GHRS intermediate resolutions are extremely small (Cardelli, Ebbets, & Savage 1993). The individual FP-Split subexposures were merged using the "centroid merge" procedure, which aligns the subexposures by calculating the central velocities of narrow interstellar lines in the spectra.

In Table 2 we list the wavelength, f-value, equivalent width and $\pm 1\ \sigma$ error, and velocity integration range for all interstellar lines identified in our G160M spectra of HD 116852. Table 2 also contains information about the ionization potentials for creation and destruction of each species and the

TABLE 1

GODDARD HIGH-RESOLUTION SPECTROGRAPH OBSERVATIONS HD 116852

Observation[a] Identification	Grating	Resolution[b] FWHM (km s^{-1})	Wavelength Coverage (Å)	Exposure[c] Time (s)	Velocity[d] Shift (km s^{-1})	Species Observed
Z15A010AT	G160M	18	1232.8–1268.9	588.8	0	C I, C I*, C I**, Mg II, Ge II, Si II, S II, N V
Z15A010DM	G160M	16	1369.9–1405.6	1280.0	0	Ni II, Si IV
Z15A010GM	G160M	14	1520.9–1556.1	1612.8	0	Si II, C IV
Z15A010JM	G160M	11	1842.8–1876.8	819.2	-5	Al III

[a] *HST* archive identification. All observations were obtained with the star in the small science aperture (SSA: $0''.25 \times 0''.25$) using step-pattern 6 (two substeps per diode), comb-addition, and the FP-Split = 4 procedure to reduce fixed-pattern noise.

[b] Approximate nominal resolution for the central wavelength using the SSA as listed in the Goddard High-Resolution Instrument Handbook (Duncan 1992).

[c] Total on-spectrum exposure time.

[d] Velocity shift required to bring the spectra into the heliocentric velocity reference frame. An additional shift of -6.4 km s^{-1} s^{-1} for all observations was required to bring the heliocentric velocities into the local standard of rest velocity reference frame.

1994ApJ...431..201S

TABLE 2

EQUIVALENT WIDTHS OF THE ABSORPTION LINES SHOWN IN FIGURE 1

ION	IP (eV)[a] (x^{i-1})	IP (eV)[a] (x^i)	λ[b] (Å)	f-VALUE[c]	$W_\lambda \pm 1\ \sigma$ (mÅ)	INTEGRATION RANGE (km s^{-1})	S/N	NOTES
C I	...	11.26	1260.735	3.937 (−2)	48.6 ± 3.3	−25 to +30	48	1, 6
C I*	...	11.26	1260.927	1.312 (−2)	24.6 ± 4.8	−40 to +50	48	2, 6
(blend)			1260.996	9.840 (−2)				
			1261.122	1.640 (−2)				
C I**	...	11.26	1261.426	9.837 (−3)	2.9 ± 2.9	−40 to +25	48	3, 6
(blend)			1261.552	2.951 (−2)				
C IV	47.89	64.49	1548.195	1.908 (−1)	321.7 ± 4.8	−110 to +70	55	9
			1550.770	9.522 (−2)	204.6 ± 4.7	−110 to +70	87	9
N V	77.47	97.89	1238.821	1.570 (−1)	59.2 ± 9.0:	−110 to +70	42	6
			1242.804	7.823 (−2)	30.7: ± 6.2:	−110 to +70	60	6
Na I	...	5.14	5589.950	6.311 (−1)	353.2 ± 3.2	−45 to +30	87	4, 7
			5895.924	3.180 (−1)	279.6 ± 3.7	−45 to +30	87	4, 7
Mg II	7.65	15.04	1239.925	1.220 (−3)	44.6 ± 2.7	−55 to +30	68	7
			1240.395	6.120 (−4)	30.5 ± 2.4	−55 to +30	71	7
Si II	8.15	16.34	1260.422	1.007 (0)	466.8 ± 5.0	−120 to +60	48	5, 6, 7
			1526.707	2.303 (−1)	451.0 ± 6.8	−120 to +60	48	7
Si IV	33.49	45.14	1393.755	5.140 (−1)	206.3 ± 6.3	−110 to +70	57	7
			1402.770	2.553 (−1)	123.9 ± 5.9	−110 to +70	85	7
P II	10.49	19.72	1532.533	7.610 (−3)	22.1 ± 3.6	−55 to +30	57	8
S II	10.36	23.33	1250.584	5.453 (−3)	185.2 ± 3.8	−90 to +50	58	7
			1253.811	1.088 (−2)	234.4 ± 4.1	−90 to +50	52	7
			1259.519	1.624 (−2)	256.3 ± 2.6	−90 to +50	62	7
Al III	18.83	28.48	1854.716	5.602 (−1)	208.6 ± 8.9	−80 to +40	32	
			1862.790	2.789 (−1)	126.2 ± 11.7	−80 to +40	34	
Ca II	6.11	11.97	3933.663	6.346 (−1)	422.8 ± 6.6	−75 to +45	38	4
Ni II	7.64	18.17	1370.132	1.309 (−1)	84.8 ± 4.1	−90 to +50	70	8
Ge II	7.90	15.93	1237.059	8.756 (−1)	15.5 ± 3.4	−55 to +30	45	8

[a] Creation and destruction ionization potentials from Moore 1970.

[b] Rest vacuum wavelengths from data compilation prepared by Morton 1991.

[c] f-Values from data compilation prepared by Morton (1991). Note that the f-value for Ge II λ1237.059 has been increased by a factor of 10 because of an error in Morton's table (see Hobbs et al. 1993). For Mg II, we use the empirical f-values recommended by Sofia et al. 1994. Numbers in parentheses indicate base 10 exponent.

[d] Notes: (1) The C I λ1260.735 line lies in the wing of the Si II/Fe II blend at 1260.4 Å. (2) The listed equivalent width is the total equivalent width for the C I* blend near 1261 Å and the listed velocity range is centered on the 1260.996 Å line. (3) The listed equivalent width is the total equivalent width for the C I** blend near 1261. 5 Å and the listed velocity range is centered on the 1261. 552 Å line. (4) Profile from Sembach et al. 1993. (5) Blend with Fe II λ1260.533. (6) Additional continuum placement uncertainties may exist. (7) Unresolved saturated structure exists. The adopted correction procedures are described in the text. (8) Unresolved saturated structure may exist. (9) Line lies on a well-developed stellar P-Cygni profile which provides a smooth continuum.

approximate signal-to-noise ratios measured in the continuum adjacent to each line. We measured equivalent widths and errors for the interstellar lines according to the stellar continuum fitting and error propagation methods outlined by Sembach & Savage (1992). We used only data points having $|v_{\rm LSR}| \leq 250$ km s^{-1} in estimating the continua, except for the strong Si II λ1260 line for which we included some points outside this range. Any errors due to background subtraction uncertainties are very small; we estimate them to be less than 0.5% of the listed equivalent widths. The velocity integration ranges listed in column (7) of Table 2 extend approximately 5 to 15 km s^{-1} past the velocities where the absorption line wings re-enter the continuum. We plot continuum normalized intensities of the interstellar lines as a function of LSR velocity in Figure 1. The additional optical observations of Na I λλ5889, 5895 and Ca II λ3933 have a resolution of 4.4 km s^{-1} (FWHM) and come from Sembach, Danks, & Savage (1993).

The heliocentric velocities provided for each observation by the standard wavelength calibrations and *HST* Doppler compensator have a 1 σ uncertainty of ±0.5 diode (~10 km s^{-1}). We checked the internal consistency of this wavelength scale by comparing the relative velocities of both high- and low-ionization interstellar lines in the individual observations. The steep negative velocity wings of the strong Si II λλ1260 and 1526 lines indicated a (default) shift of 0 km s^{-1} between the 1200 and 1500 Å spectral region observations. An additional check using the cores of the weak Ge II λ1237 and P II λ1533 lines confirmed this conclusion. Comparison of the Ni II λ1370 and Mg II λ1239 lines did not reveal any serious velocity discrepancies between the 1200 Å and 1400 Å spectral regions. We also matched the velocities of the Si IV λλ1393, 1402 and C IV λλ1548, 1550 lines observed with the *IUE* (Sembach & Savage 1992) to the GHRS observations and found the velocities of the lines in the two data sets to be internally consistent to within 3 km s^{-1}. We applied the same test to the Al III λλ1854, 1862 lines and found a modest (−5 km s^{-1}) shift was required for the GHRS data to make the velocities of the two data sets consistent. We added a shift of −6.4 km s^{-1} to all heliocentric velocities to transform them into local standard of rest velocities according to the LSR reference system described by Mihalas & Binney (1981). All velocities referred to in later sections of this paper are in the LSR reference frame.

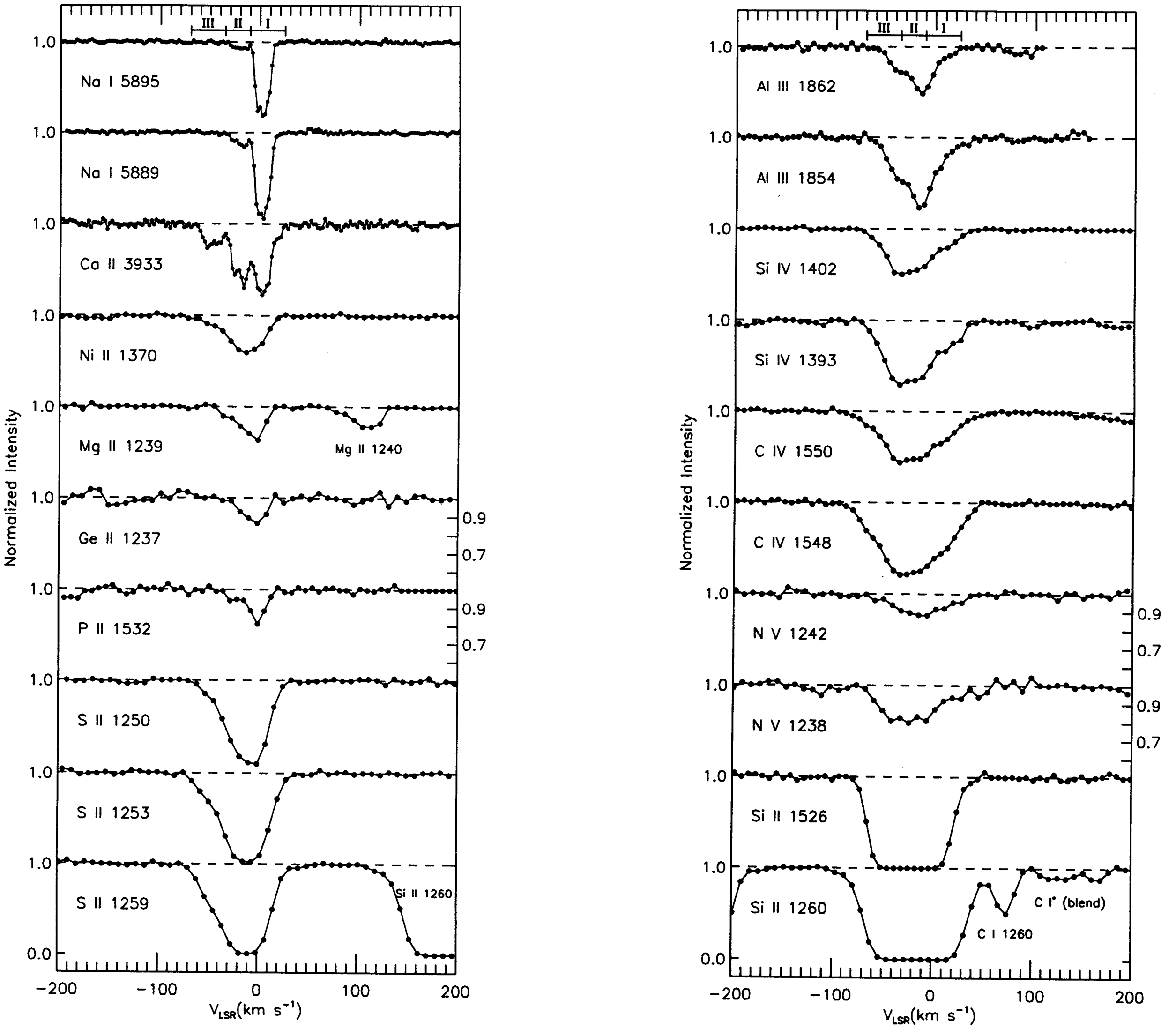

FIG. 1.—Normalized intensity vs. LSR velocity for the interstellar lines identified in the GHRS G160M observations listed in Table 1. The zero levels for each line coincide with the unity intensity level of the line below, except in a few cases where the vertical axes are expanded by a factor of 2 to show the absorption structure better. The lines are arranged in approximate order of increasing ionization potential except for the strong Si II λλ1260, 1526 lines which are plotted below the high ion profiles. We indicate the scales of the expanded plots on the right hand sides of the panels. The GHRS data have resolutions of 11 to 18 km s^{-1} (FWHM). The optical Na I and Ca II data are from Sembach et al. (1993) and have a resolution of 4.4 km s^{-1} (FWHM). The velocity intervals discussed in the text are displayed at the top of each panel.

3. ABSORPTION LINE DESCRIPTION

3.1. *Stellar Overview*

Morgan, Code, & Whitford (1955) classified HD 116852 as an O9 III star, and we find that this optical classification is consistent with the observed features in the UV portion of the HD 116852 spectrum. Figure 2 contains a comparison of the primary photospheric and stellar wind lines for HD 116852 and an O9 III standard star (HD 37043, ι Ori). We prepared this figure using high-dispersion *IUE* archival data processed with the method outlined by Sembach & Savage (1992). We smoothed the spectra with a 0.25 Å boxcar filter to reduce noise and emphasize the general structure present in the stellar lines. The most important stellar lines, which are identified in the figure caption, are labeled "L" or "T" depending upon whether the line strengths are primarily luminosity or temperature sensitive. Prominent interstellar lines are identified "IS" near the HD 116852 spectrum. The projected rotational velocities of HD 116852 ($v \sin i = 115$ km s^{-1}; Balona 1975) and ι Ori ($v \sin i = 122$ km s^{-1}; Hoffleit & Jaschek 1982) are comparable, and the strengths of the photospheric lines for both stars are typical of those for O9 III stars (see Prinja 1990 for equivalent widths of some of these stellar lines).

The level of development of the HD 116852 UV wind lines is also commensurate with a spectral type of O9 III. In Figure 3 we show the GHRS G160M observations of the stellar high ion profiles for HD 116852 as a function of wavelength. The C IV P-Cygni profile is well developed and provides a smooth continuum to measure the interstellar C IV lines against. We measure a maximum C IV stellar wind absorption velocity of -2580 km s^{-1}, which agrees well with the value of -2600 km s^{-1} found by Howarth & Prinja (1989; see also Prinja, Barlow,

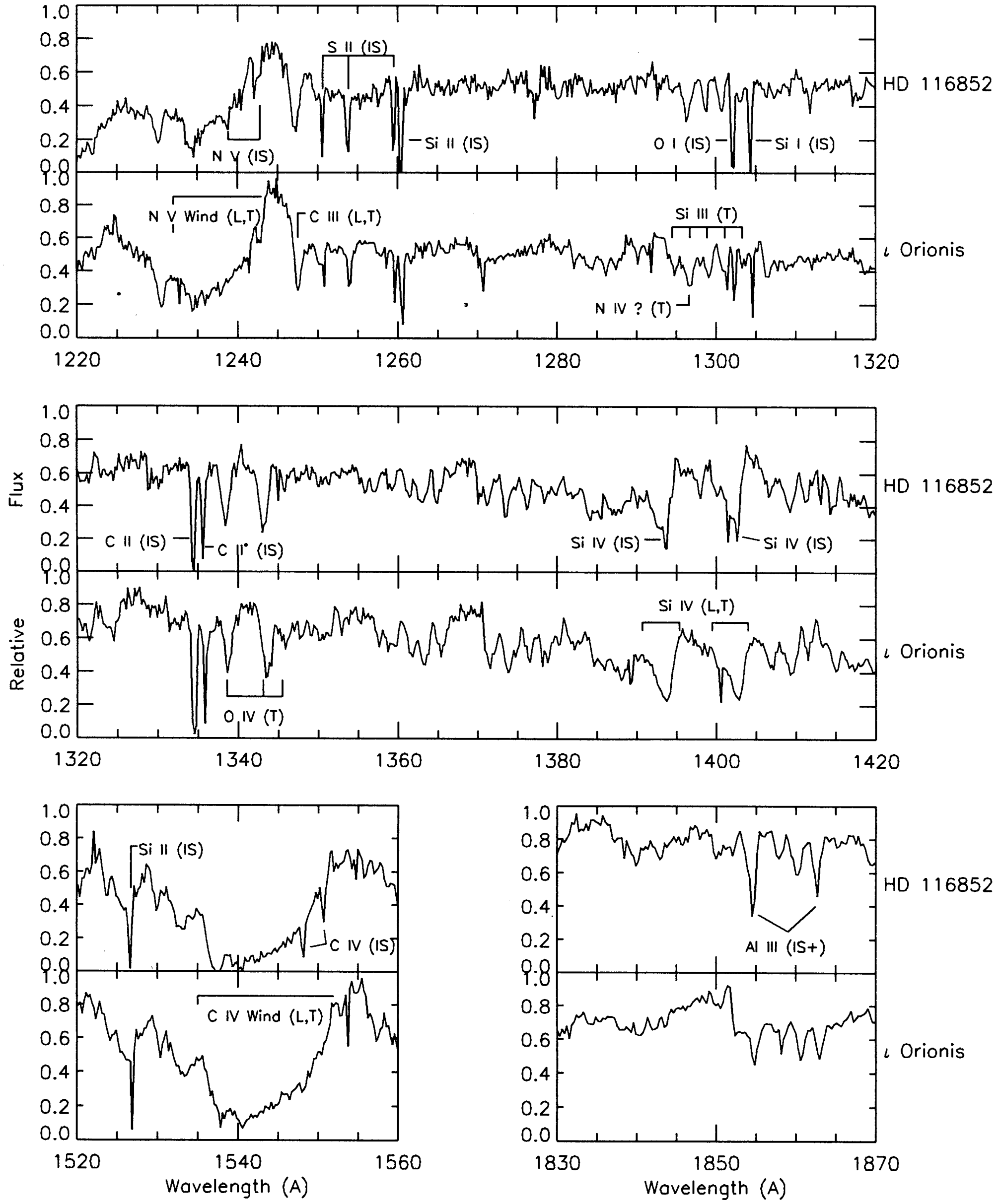

FIG. 2.—Relative flux vs. wavelength for selected ultraviolet spectral regions of HD 116852 and ι Ori. We obtained these single well-exposed high dispersion spectra from the *IUE* data archives and smoothed them with a 0.25 Å boxcar filter to reduce noise and emphasize the stellar structure present in the spectra. Various interstellar (IS) lines discussed in the text are labeled in the panels containing the HD 116852 data. Stellar lines sensitive to temperature (*T*) and luminosity (*L*) are labeled in the panels containing the ι Ori data. These stellar lines include the Si IV, C IV, and N V wind lines discussed in the text as well as the C III λ1247 line, the Si III λ1300 multiplet (λλ1294.5, 1296.7, 1298.9, 1301.1, and 1303.3), and the O IV λ1342 multiplet (λλ1338.6, 1343.0, and 1345.5).

& Howarth 1990). Several narrow absorption-line component (NAC) groupings are present in the C IV stellar wind profiles at LSR velocities of −2270, −2140, and −2045 km s^{-1}. Ignoring the NAC absorption, the intensity at maximum absorption at large velocities in the C IV P-Cygni profile drops to 4% of the peak emission intensity.

The N V P-Cygni profile is less developed than the C IV profile and decreases to 22% of the peak emission intensity. As a result, there is considerably more structure from photospheric absorptions superposed on the P-Cygni structure of the N V lines than there is for the C IV lines. This is generally true for O9 III stars; well-developed N V P-Cygni profiles do not occur for spectral types later than O8 (Abbott, Bohlin, & Savage 1982; Walborn, Nichols-Bohlin, & Panek 1985). Undulations in the stellar continuum caused by photospheric absorption complicate continuum placement for the interstellar N V lines, and our analysis of the interstellar N V lines is subject to some uncertainties resulting from our choice of the stellar continuum (see § 3.2). The N V observation shown in Figure 3 does not extend to large enough negative velocities for us to comment on the maximum stellar N V absorption velocity or detection of N V absorption associated with the NAC groupings seen in C IV.

The Si IV stellar wind profiles are less developed than either the C IV or N V profiles and reach an absorption depth of about 55% of the stellar continuum intensity. There is little or

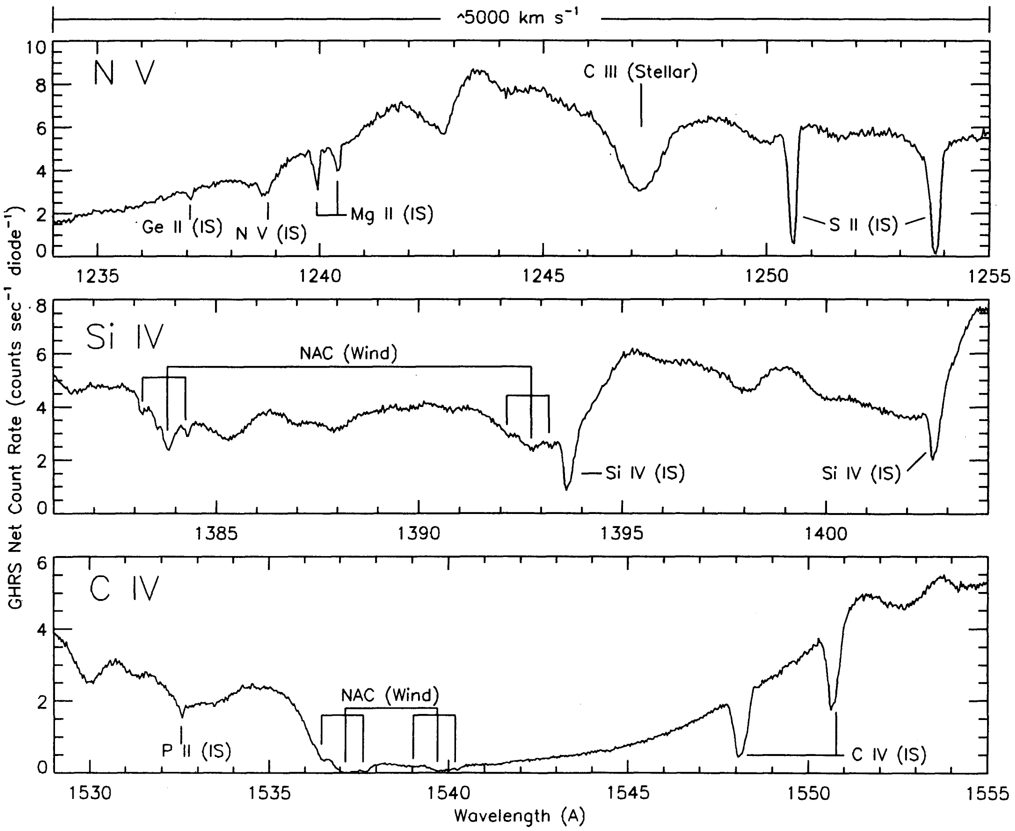

FIG. 3.—GHRS G160M spectra illustrating net count rate vs. wavelength for the HD 116852 Si IV, C IV, and N V spectral regions. The illustrated wavelength range spans approximately 5000 km s^{-1} in each case. Various interstellar lines listed in Table 2 are indicated below each spectrum. In most cases, the interstellar lines are quite distinct from the broader stellar absorption profiles, with the notable exception of the N V λλ1238, 1242 lines. The C IV stellar wind P-cygni profile is well developed, while the N V and Si IV stellar wind profiles are less developed. The groups of NACs at large negative velocities (~ -2000 to -2200 km s^{-1}) in the Si IV and C IV panels are due to absorption features within the stellar wind surrounding the star.

no emission. O9 III stars exhibit Si IV absorption troughs of this type, and it is not until earlier spectral types or larger luminosities that the Si IV profiles have emission peaks (Walborn & Panek 1984). Continuum placement is simpler for the interstellar Si IV lines than for the interstellar N V lines because the broad, photospheric absorption is pronounced enough to provide a smoothly varying continuum for the narrower interstellar Si IV absorption profiles. The NACs identified in the C IV wind profiles are also present in the stellar Si IV profiles, which extend to about -2400 km s^{-1}. The Si IV λ1402 NACs occur at LSR velocities of -2270, -2140, and -2045 km s^{-1}, which correspond to velocities of -337, -207, and -112 km s^{-1} with respect to the Si IV λ1393 interstellar absorption. Fortunately, these wind features do not adversely affect our investigation of the interstellar Si IV lines.

Hill, Kilkenny, & Van Breda (1974) measured the *UBV* colors of HD 116852 and found $V = 8.47$, $B-V = -0.09$, and $U-B = -0.99$. These colors lead to a Balmer-jump index, $Q = (U-B) - 0.72(B-V) = -0.92$, representative of stars with spectral types near O8 or O9 (see Mihalas & Binney 1981). Combining these colors with the absolute magnitude scale for O stars derived by Walborn (1973) and the intrinsic O star colors given by Johnson (1963), we calculate a spectroscopic distance of 4.8 kpc for HD 116852. In computing this distance, we used the relation $A_v = 3.1\ E(B-V)$, the standard diffuse interstellar extinction in the visual band (Savage & Mathis 1979). The LSR radial velocity of -47 km s^{-1} found for HD 116852 by Feast, Thackeray, & Wesselink (1963) yields a kinematic distance comparable to $d \approx 4.8$ kpc (see § 6.1 for a discussion of the relationship between velocity and distance for the sight line).

3.2. *Interstellar Overwiew*

3.2.1. *Low Ionization Lines*

We have divided the structure visible within the low ion ($IP_{[\mathrm{I-II}]} < 13.6$ eV) lines shown in Figure 1 into the three general velocity intervals marked above the Na I profiles. Ranked in order of decreasing absorption strength, they are as follows: I: $-10 < v \leq +25$ km s^{-1}, II: $-35 < v \leq -10$ km s^{-1}, and III: $-70 < v \leq -35$ km s^{-1}. Each of these intervals contains several components seen in high resolution measurements of the optical Na I and/or Ca II lines. The Na I absorption is confined exclusively to intervals I and II at velocities of -25.8, -16.2, -2.9, $+2.7$, and $+7.6$ km s^{-1}, but Ca II components occur in all three intervals at velocities of -54.3, -42.8, -26.2, -16.4, $+2.3$, and $+19.9$ km s^{-1} (Sembach, Danks, & Savage 1993). Only the very strong lines of Si II λλ1526, 1260 and S II λλ1253, 1259 or the lines of highly refractory elements such as Ni II λ1370 and Ca II λ3933 show significant absorption in low ion velocity interval III. The largest fraction of the low ion absorption (reaching a high of 85% for Na I) occurs in velocity interval I.

In most cases, the low-ionization interstellar lines are readily separable from the underlying stellar photospheric absorption. The large rotational velocity of the star ($v \sin i = 122$ km s^{-1}) produces photospheric lines broader than all but the strongest low ion interstellar lines. The strongest low ion lines observed, Si II λλ1260 and 1526 Å, have steep absorption walls that clearly indicate that almost all the neutral gas absorption in the diffuse interstellar medium lies between -70 km s^{-1} and $+40$ km s^{-1}. The Si II λ1260 line is a blend of Si II λ1260.422 and Fe II λ1260.533, which leads to the large positive velocity extent of this line compared to the Si II λ1526 line.

The narrow absorption feature at $+75$ km s^{-1} in the Si II λ1260 profile illustrated in Figure 1 is due to C I λ1260.735 absorption. Additional lines of C I* are seen in the same spectrum at velocities of $+120$, $+137$, and $+167$ km s^{-1}. Although not illustrated, weak lines of C I** λλ1261.426, 1261.552 are also present in the Si II λ1260 spectrum.

3.2.2. *Ionized Gas Lines*

The Si IV, C IV, and N V absorption profiles illustrated in Figure 1 are unmistakably distinct in appearance from the Al III and low ion profiles. The absorption strength of the high ion lines increases to negative velocities, and unlike the low ion lines, the majority of the absorption occurs in velocity intervals II and III. Maximum absorption depths for the Si IV and C IV lines occur near $v(\tau_{\max}) = -35$ km s^{-1}, which is a velocity where the low ion absorption traced by Mg II, P II, Ca II, and Ni II recovers nearly to the continuum. The Si IV, C IV, and N V lines have FWHM ≈ 62, 74, and 60 km s^{-1}, respectively, and extend to larger positive velocities than low ion lines having comparable optical depths. Some absorption visible in the broad negative velocity wings of the strong low ion profiles may be related to the higher ionization gas (compare the Si II and S II lines with the Si IV lines).

Continuum placement for the N V lines is somewhat subjective, but can be simplified by comparing the shape of the continuum to that seen in other species. The broad, underlying feature present in the N V spectra region shown in Figure 3 is due to photospheric N V. It has a shape and velocity centroid similar to those found for the stellar He I λ5875 line by Sembach, Danks, & Savage (1993). Using the He I line as a guide in placing the continuum, we removed this absorption before producing the normalized version of the interstellar N V profile shown in Figure 1. Some additional uncertainties may exist in the derived N V continua, particularly on the negative velocity side of the profiles, and for this reason we concentrate most of the remaining analysis on the stronger λ1238 line. The N V equivalent widths listed in Table 2 are approximately a factor of 2 smaller than those reported from *IUE* measurements by Sembach & Savage (1992). We attribute this difference to the blending of stellar absorption in the interstellar profile measured in the previous lower S/N *IUE* study.

Al III represents an intermediate case between the low and high ions. The Al III lines show a major absorption enhancement near -15 km s^{-1} that is present, but much less pronounced, in the Si IV and C IV profiles. Maximum Al III absorption occurs within velocity interval II at $v(\tau_{\max}) = -15$ km s^{-1}, compared to $v(\tau_{\max}) = +2$ km s^{-1} for the lower ionization lines. The velocity differences seen in the low, intermediate, and high ions along the sight line are due to the differing distributions and ionization conditions of the gases containing these species as discussed in §§ 6 and 7.

4. SIGHT LINE SYNOPSIS

4.1. *General Properties*

Diplas & Savage (1994) determined a neutral hydrogen column density of $\log N(\text{H I}) = 20.96 \pm 0.08$ toward HD 116852 based upon an analysis of the damped Lyα absorption observed with the *IUE* satellite. This H I column density implies an average spatial density of only 0.06 atoms cm^{-3} over the length of the sight line. Using the Na I column density derived in § 5 and the approximate Na I to H I relationship, $\log N(\text{Na I}) = \log N(\text{H I}) - 8.16$ (Diplas & Sembach 1994; see also Ferlet, Vidal-Madjar, & Gry 1985), we predict that most of the neutral hydrogen along the sight line is associated with lower velocity gas near the Galactic plane at velocities between -45 and $+30$ km s^{-1} (see Fig. 1).

Kerr et al. (1986) produced H I maps covering this longitudinal direction within ±10° of the Galactic plane. At $b = -10°$ and $l = 305°$, the H I column density per unit velocity drops by a factor of 50 from $v = 0$ to -50 km s^{-1}. The maps do not extend to $b < -10°$, but the general trend within 10° of the plane indicates that N(H I) per unit velocity is less than 2×10^{18} [atoms cm^{-2} (km s^{-1})$^{-1}$] for $v < -40$ km s^{-1} and $v > 20$ km s^{-1}. This conclusion is supported by the moderate latitude ($-32° \leq b \leq -17°$) H I survey maps presented by Colomb, Gil, & Morras (1976) and is consistent with the absence of Na I absorption in velocity interval III.

Larger scale structures, such as spiral arms, are present in the Galactic disk in the general direction of HD 116852. The Carina link of the Sagittarius spiral arm lies at a distance of approximately 1.5 to 2.0 kpc (Courtès et al. 1970; Bok 1971). Gas and H II regions within the Sagittarius-Carina spiral arm link have velocities of -20 to -30 km s^{-1} at $l = 305°$ (Courtès 1972; Rickard 1974). The Norma-Centaurus spiral feature is also present in this direction, but is distinct from the Carina link in both distance and velocity. Located at a distance of more than 3.5 kpc, the Norma-Centaurus arm is characterized by gas with velocities between -30 and -50 km s^{-1} (Courtès 1972; Rickard 1974).

The HD 116852 sight line passes under the Sagittarius-Carina link and Norma-Centaurus spiral arm at z-distances of about -500 pc and -1000 pc, respectively. Neutral gas associated with these arms is confined to within several degrees (~200 pc) of the Galactic plane (see for example, the H I maps presented by Kerr et al. 1986), but ionized spiral arm gas may exist at larger distances from the main gas concentrations within the arms. Theoretical models of highly ionized gas flows associated with Galactic chimneys (Norman & Ikeuchi 1989), Galactic fountains (Bregman 1980; Shapiro & Benjamin 1993), and shocks produced by Galactic density wave perturbations (Martos & Cox 1994) predict the existence of highly ionized spiral arm gas up to z-distances of at least 1 kpc. The strong absorption near -15 km s^{-1} in the Al III profiles shown in Figure 1 is presumably associated with gas in the Sagittarius-Carina link, but it is less certain whether the remaining Al III or higher ion absorption can be attributed to such gas (see §§ 6 and 7).

The HD 116852 sight line passes through the southern portion of Radio Loop I, which is thought to have been created by past supernova activity in the region (Iwan 1980). Portions of Radio Loop I are visible in H I surveys (Heiles 1982) and X-ray emission maps (McCammon 1984), and models of the radio continuum emission associated with the loop indicate gas at the edge of the loop should have an expansion velocity of approximately 25 km s^{-1} (Berkuijsen, Haslam, & Salter 1971). HD 116852 lies on the edge of the Galactic center *M* band (0.4–1.1 keV) enhancement seen in X-ray emission maps of the sky (Nousek et al. 1982; McCammon et al. 1983). An absorption optical depth of unity occurs in this band for $N(\text{H I}) \sim 10^{21}$ cm^{-2}, a value comparable to the integrated H I column density along the line. Therefore, some of the high ion absorption seen along the sight line could be associated with the *M* band emission, even if it is located at large distances. However, recent measurements of the high ion lines toward 3C 273 (Burks et al. 1991; Savage et al. 1993) demonstrate that sight lines passing through Loop I have greater high ion abundances than "average" halo sight lines toward the Magellanic Clouds. For the 3C 273 sight line, Savage et al. (1993) found $N(\text{C IV})/N(\text{Si IV}) \approx 6.8$ and $N(\text{C IV})/N(\text{N V}) \approx 5.9$. For HD 116852 we find $N(\text{C IV})/N(\text{Si IV}) \approx 3.9$ and $N(\text{C IV})/N(\text{N V}) \approx 4.5$, which are values similar to the Galactic average found by Sembach & Savage (1992) (see § 7.3).

Several "Galactic worm" candidates are located near the Galactic plane in the general direction of HD 116852 (Koo, Heiles, & Reach 1992). Of the five superstructure candidates having negative latitudes and longitudes between 295° and 315°, GW 304.6 − 7.8 lies closest (in angle) to the HD 116852 sight line. The bubble is confined to $b > -10°$ in H I and *IRAS* 100 μm emission and has a very uncertain distance estimate of 10 kpc. The remaining four bubbles have H I emission that is even more confined to the Galactic plane.

Fourteen H II regions have been cataloged at negative latitudes and longitudes between 300° and 310° by Marsálková (1974). All have angular diameters less than a few degrees in size, and in most cases the H II regions are only tens of arcminutes in diameter. These H II regions do not contribute to the high ion absorption in our study unless the associated regions bearing the highly ionized gas are many times the angular size of the radio and optical regions, which seems improbable.

4.2. *The Circumstellar Environment*

Most of the nonstellar high ion gas absorption observed toward HD 116852 must be interstellar in nature and cannot be attributed to the circumstellar environment of the star. Two potential sources of circumstellar contamination exist: photoionization of gas in the H II region and collisional ionization in a wind-blown bubble interface. If gas near HD 116852 has a velocity similar to that of the star (a reasonable assumption for gas participating in Galactic rotation, see § 6.1), circumstellar gas will have line-of-sight velocities that are blueshifted relative to the stellar velocity (i.e., $v < v_* = -47$ km s^{-1}) due to H II region or circumstellar bubble expansion. The low and intermediate ionization species associated with these types of regions have steeply declining absorption strengths for $v < -47$ km s^{-1}. It is also typical for H II regions to have turbulent velocities ranging from 5 to 15 km s^{-1} (Reynolds 1985; Steigman, Strittmatter, & Williams 1975), which are insufficient to produce the large negative velocity extension of the high ion profiles, much less their overall widths.

Cowie, Taylor, & York (1981) have estimated the column densities of Si IV and C IV in H II regions surrounding hot stars based upon LTE stellar atmosphere models (see also Black et al. 1980). Assuming an effective surface temperature of 32,500 K (Howarth & Prinja 1989), the expected column densities due to photoionization for a nebula having a uniform electron density $n_e = 1$ cm^{-3} are $N(\text{Si IV}) \approx 7.4 \times 10^{14}$ cm^{-2} and $N(\text{C IV}) \approx 2.2 \times 10^{13}$ cm^{-2}; the column densities scale as $n_e^{1/2}$. Although not explicitly calculated, the expected value of $N(\text{N V})$ due to photoionization is much smaller than these estimates (by orders of magnitude) because of photon absorption by the stellar He II absorption edge at 54 eV (see, for example, the photoionization calculations given by Dupree & Raymond 1983). For $n_e = 1$ cm^{-3}, the predicted column density of Si IV is almost two orders of magnitude larger than the observed amount for $v < -47$ km s^{-1}, while the predicted amount of C IV is within 15% of the observed amount for $v < -47$ km s^{-1}. Sembach, Savage, & Jenkins (1994) find similar large disagreements between observations and theory for the H II region surrounding ζ Oph. It is possible that the assumed EUV energy distributions for hot stars are in error.

Even though these predicted column densities are comparable to, or larger than, the observed Si IV and C IV values, an H II region interpretation alone cannot explain the large negative velocity extensions of the observed profiles. The H II region interpretation has difficulty accounting for the small amounts of Al III seen at these velocities. Sembach, Savage, & Jenkins (1994) found that $N(\text{Si IV})/N(\text{Al III}) \approx 2.0$ in the H II region surrounding ζ Oph, an O9.5 IV star with an effective temperature near 32,000 K. For HD 116852, we find $N(\text{Si IV})/N(\text{Al III}) \approx 4.3$ for $v < -47$ km s^{-1}. These two measurements may be reconciled by requiring the gas phase abundance of silicon relative to aluminium be a factor of 2 larger toward HD 116852 than toward ζ Oph. Given the small amount of observed Si IV compared to the predicted amounts and the observed velocity structure of the Al III and Si IV lines, it is unclear whether any of the observed Al III and Si IV absorption arises in an H II region around HD 116852. However, it appears very unlikely that photoionization in the H II region is producing C IV and N V near $v \approx -47$ km s^{-1}.

Stellar winds in the circumstellar environments of hot stars alter the ionization structure of normal radiation bounded H II regions. HD 116852 has a stellar wind with a mass-loss rate $\dot{M} = 2.0 \times 10^{-7}$ $M_\odot$ yr^{-1} and a terminal velocity $v_\infty \approx 2600$ km s^{-1} (Howarth & Prinja 1989). Weaver et al. (1977) derived an expression for the expected high ion column densities produced by collisional ionization in the conductive interface located where the stellar wind abuts the surrounding ISM (see their eq. [50]). They concluded that incorporating a time dependent ionization balance, the effects of radiative losses, and a spherical geometry increases the expected column densities by approximately a factor of 1.5 over the initial estimate given by Castor, McCray, & Weaver (1975). After further updating their results for the cosmic abundances given by Anders & Grevesse (1989)[4] and using the wind parameters listed above, we estimate interface column densities $N(\text{ion}) \approx C\, n_0^{9/35} t_6^{8/35}$ cm^{-2}, where n_0 is the density of the ambient ISM in cm^{-3}, t_6 is the age of the bubble in millions of years, and $C = 2.5 \times 10^{11}$, 3.8×10^{12}, and 1.6×10^{12} for Si IV, C IV, and N V, respectively. A "typical" value of $n_0 t_6$ is unity, but a factor of 100 difference in this quantity affects the resulting column densities by approximately a factor of 3. The predicted amounts of high ion gas are factors of 16.4, 6.6, and 3.1 less than the observed column densities of Si IV, C IV, and N V for $v < -47$ km s^{-1}. Thus, only a small fraction of the absorption

---

[4] The cosmic oxygen abundance given by Anders & Grevesse (1989), $X(\text{O}) = 8.5 \times 10^{-4}$, is about a factor of 2 larger than the value of 4.4×10^{-4} used by Weaver et al. (1977). The solar carbon, nitrogen, and silicon abundance estimates used by Weaver et al. differ by less than 20% from the values adopted here.

along the sight line could be produced in an evaporative interface in the immediate vicinity of the star.

Perhaps the most likely absorption structure seen in the high ion profiles associated with circumstellar material is the C IV absorption observed near $v_{\rm LSR} = -68$ km s^{-1} that is not modeled well by the interstellar gas distribution model discussed in § 6. Hot, collisionally ionized gas associated with a circumstellar shell plowing into the surrounding ISM is a possible site for the C IV absorption. The C IV column density near $v_{\rm LSR} = -68$ km s^{-1} associated with this absorption is N(C IV) $\approx 8.9 \times 10^{12}$ cm^{-2}. Using the results of Castor et al. (1975) and assuming that the expanding shell is moving at 20 km s^{-1} with respect to the star, we find $n_0^{1/5}t^{2/5} \approx 1.1 \times 10^5$, where n_0 (cm^{-3}) is the density of the ambient ISM encountered by the outer bubble shell containing the high ions and t (years) is the age of the shell (see eqs. [4] and [5] of Sembach, Savage, & Jenkins 1994). For values of n_0 ranging from 0.1 to 4.0, $t \approx (0.8\text{–}1.8) \times 10^5$ years. Stars with large masses have short stellar wind lifetimes ($\sim 10^5$ to 10^6 years). HD 116852 has a mass of approximately 28 $M_\odot$, and therefore the age of the shell implied by the C IV absorption velocity represents a significant fraction of the stellar wind lifetime.

5. ANALYSIS

5.1. *Apparent Column Density Profiles and Integrated Column Densities*

One of the best ways to analyze the high quality Al III, Si IV, C IV, and N V lines shown in Figure 1 is to convert the absorption profiles into profiles of apparent column density as a function of LSR velocity. The conversion allows for the direct assessment of a physically meaningful quantity, the column density (or scaled optical depth) at a given velocity. Comparisons of the apparent column density profiles of different species then yield information that can be used to interpret the physical and kinematical nature of the absorption along the sight line. This is particularly useful for the HD 116852 sight line since the velocity of the absorption also provides some information about where along the sight line the absorption arises.

A continuum normalized absorption profile, $I(v)$, of the type shown in Figure 1 for a line having a rest wavelength, λ, and an oscillator strength, f, can be converted to an apparent column density profile, $N_a(v)$ [atoms cm^{-2} (km s^{-1})$^{-1}$], through the following equations:

$$\tau_a(v) = \ln \frac{1}{I(v)} \tag{1}$$

$$N_a(v) = \frac{m_e c/\pi e^2}{f\lambda}\, \tau_a(v) = 3.768 \times 10^{14}\, \frac{\ln[-I(v)]}{f\lambda} \tag{2}$$

where $\tau_a(v)$ in equation (1) is the apparent optical depth of the line as a function of velocity and the variables in equation (2) represent the usual atomic constants. We call $N_a(v)$ in equation (2) an *apparent* column density per unit velocity because the original absorption line is viewed through an instrumental spread function having a finite resolution (see Table 1). Savage & Sembach (1991) have shown through numerical simulations that if the $N_a(v)$ profiles for doublet lines agree to within approximately 20%, then they do not contain unresolved saturated structure exceeding this amount, and the individual $N_a(v)$ profiles provide a reliable representation of the true column density per unit velocity convolved with the instrumental spread function.

We show the apparent column densities for the Al III, Si IV, C IV, and N V lines as a function of LSR velocity in Figure 4, where we plot weak line values of $N_a(v)$ as solid circles and strong line values as open circles. The satisfactory agreement between the $N_a(v)$ profiles within each doublet confirms that they are not seriously affected by unresolved line saturation. For N V, we illustrate only the better defined profile for the λ1238 line. The solid vertical lines indicate errors on individual points within the $N_a(v)$ profiles resulting from continuum placement uncertainties and statistical (Poisson) noise fluctuations in the line intensity values. These errors are generally larger than the differences between the profiles. Portions of the $N_a(v)$ profile for the Si IV λ1393 line lie 5% to 10% below the $N_a(v)$ profile for the weaker λ1402 line. Some saturated structure is present between -45 and -10 km s^{-1} in the stronger line profile, which may also affect the weaker line. The difference in the two profiles is readily apparent in data of this quality, but the actual amount that the weaker λ1402 line is affected is small. Numerical simulations of the type discussed by Savage & Sembach (1991) indicate that the λ1402 $N_a(v)$ profile underestimates a valid instrumentally smeared version of the true profile by less than 10% at velocities where the profiles differ.

We also illustrate the $N_a(v)$ profiles for the Mg II, P II, S II, and Ge II lines in Figure 4 with the symbol convention used for the high ion profiles. For S II solid, open, and crossed circles represent the $N_a(v)$-values for the λ1250, λ1253, and λ1259 lines, respectively. The Mg II lines clearly contain some unresolved saturated structure between -20 and $+10$ km s^{-1}. Unresolved saturated structure is also a serious problem over a large velocity range in the S II lines; the (stronger) λ1253 and λ1259 $N_a(v)$ profiles systematically underestimate the $N_a(v)$ values of the (weaker) λ1250 $N_a(v)$ profile. Given the severity of this saturated structure for the S II lines, the λ1250 $N_a(v)$ values must also be seriously affected by unresolved saturated structure at these velocities. The P II and Ge II profiles, which will be discussed in § 6, are much weaker than the Mg II and S II lines and are probably not seriously affected by unresolved saturated structure. We measure $\tau_a(v) < 0.21$ for P II and $\tau_a(v) < 0.14$ for Ge II. These values of $\tau_a(v)$ indicate that the true optical depths in the lines, $\tau(v)$, is less than unity for absorption components with $b \geq 2.3$ km s^{-1}. Therefore, unless there are very narrow components, $b < 1$ km s^{-1} [corresponding to $\tau(v) > 3$], there is little unresolved saturated structure in lines as weak as the observed P II and Ge II lines (Jenkins 1986; Savage & Sembach 1991).

We integrated equation (2) over the full velocity extent of each line (see Table 2) to obtain total apparent column density estimates for the sight line, $N_a = \int N_a(v)dv$. We list these column densities and their $\pm 1\ \sigma$ errors in columns (3) to (5) of Table 3 for the high ion lines as well as for several lower ionization lines. We compared these doublet line values of N_a to produce the adopted integrated column densities listed in columns (6) to (8) of the table according to the following scheme: (1) If the $\pm 1\ \sigma$ errors of the each doublet member overlapped the best value of the other member, we assumed the values were statistically identical, and we adopted the weak line value and error. This is true even for the Si IV lines, which contain a small amount ($<10\%$) of saturated structure. (2) If the strong line N_a-value was larger than the weak line N_a-value, we adopted the strong line results. This occurred for the N V lines, where the strong member of the doublet provides a more reliable estimate of $N_a(v)$ than the weak member. (3) If the

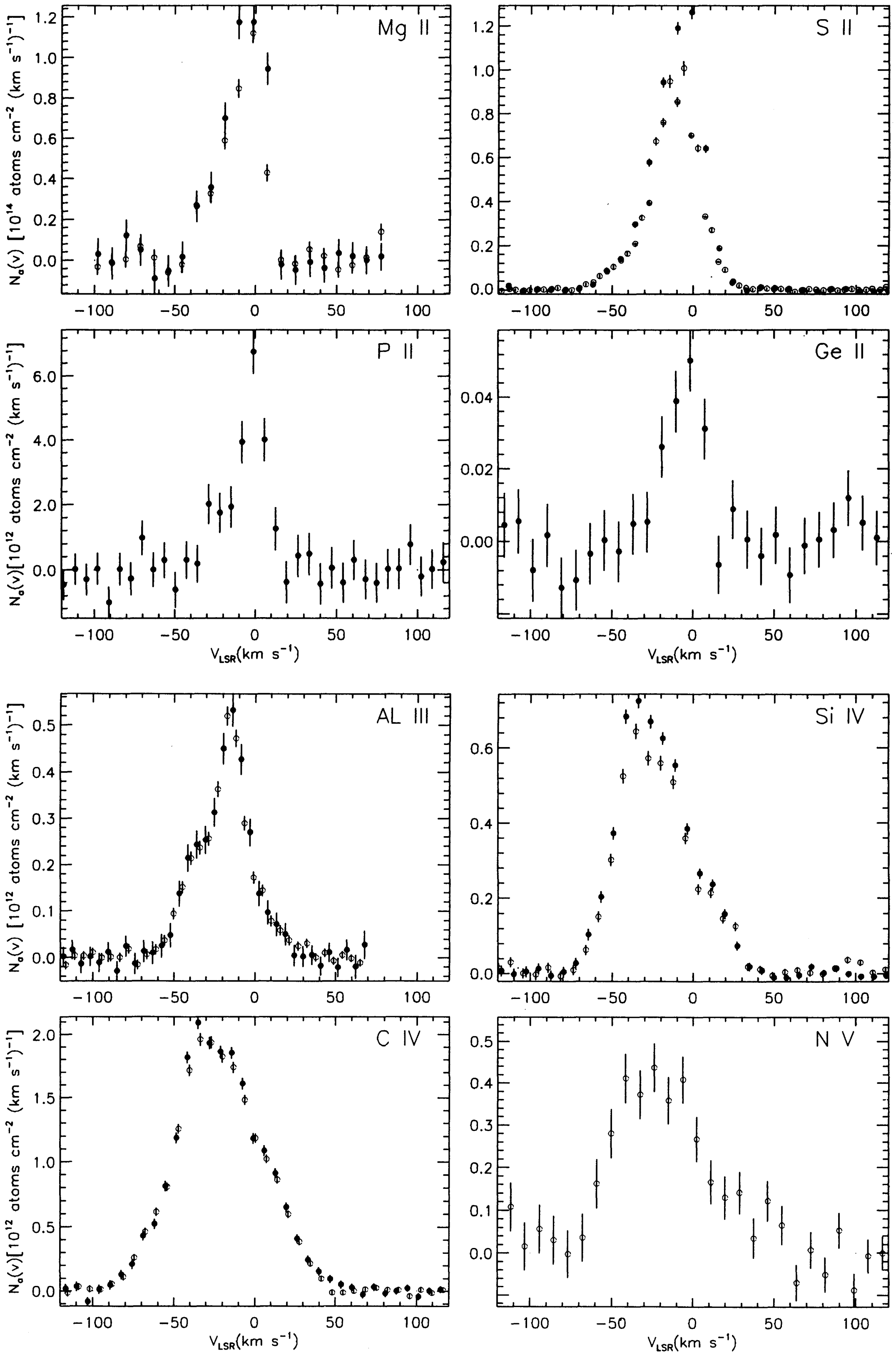

FIG. 4.—Apparent column density profiles for the Mg II $\lambda\lambda$1239, 1240; S II $\lambda\lambda$1250, 1253, 1259; *P* II λ1532; Ge II λ1237; Al III $\lambda\lambda$1854, 1862; Si IV $\lambda\lambda$1393, 1402; C IV $\lambda\lambda$1548, 1550; and N V λ1238 lines plotted as a function of LSR velocity. Filled and open circles represent values of $N_a(v)$ [atoms cm^{-2} (km s^{-1})$^{-1}$] for the weak and strong line members of each doublet, respectively. For S II, filled, open, and crossed circles indicate values of $N_a(v)$ for the λ1250, λ1253, and λ1259 lines, respectively. We have plotted only the data for the λ1238 line of N V because the λ1242 line is weak and the continuum level is less certain. The vertical error bars on each point are the errors resulting from continuum placement uncertainties and statistical noise fluctuations in the lines. For Si IV, a small amount of unresolved structure ($< \sim 10\%$) may be present in the core of the line. The remaining high ion lines do not contain unresolved saturated structure. The low ion lines contain unresolved saturated structure. Note that the S II λ1253 and λ1259 lines underestimate the values of $N_a(v)$ seen in the λ1250 line by significant amounts at most velocities, indicating that all three lines are severely affected by unresolved saturated structure.

TABLE 3

Column Densities of Selected Lines[a,b]

		log N_a			log N(Adopted)			log N(COG) [b-value (km s^{-1})]		
Ion (1)	λ (Å) (2)	($-1\ \sigma$) (3)	($+0\ \sigma$) (4)	($+1\ \sigma$) (5)	($-1\ \sigma$) (6)	($+0\ \sigma$) (7)	($+1\ \sigma$) (8)	($-1\ \sigma$) (9)	($+0\ \sigma$) (10)	($+1\ \sigma$) (11)
Na I	5889.950	12.550	12.554	12.558	12.81	12.82	12.83	12.76	12.78	12.81
Na I	5895.924	12.672	12.677	12.682				[6.1]	[6.2]	[6.4]
Mg II	1239.935	15.474	15.502	15.529	15.66	15.73	15.79	15.64	15.74	15.86
Mg II	1240.395	15.572	15.608	15.640				[3.9]	[4.8]	[6.6]
P II	1532.533	14.096	14.173	14.239	...	...	...	...	...	...
S II[c]	1250.584	15.662	15.670	15.677	15.76:	15.78:	15.79:	15.70:	15.74:	15.78:
S II	1253.811	15.565	15.573	15.580				[18.4]:	[18.8]:	[19.3]:
S II	1259.519	15.490	15.496	15.502						
Ge II	1237.059	12.033	12.138	12.223	...	...	...	...	...	...
Al III	1854.716	13.227	13.247	13.266	13.21	13.26	13.30	13.17	13.26	13.36
Al III	1862.790	13.215	13.258	13.297				[15.9]	[22.2]	[45.2]
Si IV	1393.755	13.519	13.532	13.544	13.52	13.54	13.56	13.48	13.53	13.58
Si IV	1402.770	13.523	13.544	13.564				[24.2]	[30.6]	[43.1]
C IV	1548.195	14.098	14.104	14.110	14.12	14.13	14.14	14.10	14.13	14.15
C IV	1550.770	14.107	14.117	14.127				[31.4]	[33.9]	[37.5]
N V	1238.821	13.405:	13.477:	13.539:	13.40:	13.48:	13.54:	13.41:	13.47:	13.69:
N V	1242.804	13.378:	13.477:	13.557:				[6.4]	[49.0]	[...]

[a] A 0.5% background uncertainty contributes an error of approximately 0.002 dex in log N.

[b] A colon denotes a value that may contain some additional uncertainties due to continuum placement difficulties.

[c] For S II, the λ1250 and λ1253 lines were used to compute the values of log N(Adopted) since their $f\lambda$ ratio is equal to 2. All three S II lines were used to compute log N(COG). Because of the large amount of line saturation, the S II column densities are very uncertain and should be considered as lower limits.

±1 σ errors of each member did not encompass the nominal value of the other member, we used the correction scheme outlined by Savage & Sembach (1991) to correct (increase) the weak line results. We find log N(ion) = 13.26, 13.54, 14.13, 13.48, for Al III, Si IV, C IV, and N V, respectively.

We also performed a single component, Doppler-broadened curve of growth (COG) fit to the equivalent widths of each pair of lines listed in Table 3 for comparison with the above values. The results of the fit are listed in columns (9) to (11) of Table 3. The corresponding Doppler spread parameters (b-values) are listed in square brackets below each entry. Comparisons of the relative b-values obtained for each species are useful but the absolute values have little physical meaning since the observed profiles are assemblages of multiple components. A discussion of the calculation of the errors associated with the two-dimensional ($N \times b$) chi-squared minimization used to derive the best-fit values and their errors is given by Savage, Edgar, & Diplas (1990). The adopted integrated column densities and the COG results are statistically identical; in all cases the best-fit values derived using the two techniques are within 12% of each other.

For Na I, Mg II, P II, and Ge II we find log N(ion) = 12.82, 15.73, 14.17, and 13.14, respectively. We assumed log $N \approx$ log N_a for P II and Ge II since we observed only one line of each species. For S II the saturation correction is large, and we can measure only a lower limit of log N(S II) > 15.78 (2 σ). The S II lines shown in Figure 4 and the apparent column densities listed in Table 3 indicate that even the weakest line in the S II multiplet, λ1250, underestimates the true run of $N_a(v)$. The large S II b-value found for the best-fit COG results also indicates that substantial saturation problems exist for the S II lines.

5.2. *Profile Comparisons*

In Figure 5, we compare normalized versions of the $N_a(v)$ profiles for the high and low ions. The upper panel contains the profiles for Si IV, C IV, and N V and reveals that the three ions have similar profile shapes and overall extents. The lower panel contains the profiles for P II, Al III, and C IV and illustrates the velocity offsets and shape differences that exist between the species. Errors on the profiles in the two panels can be judged by referring to Figure 4. The high ion profiles show substantial column densities out to large negative velocities, $v < -50$ km s^{-1}. The Si IV and C IV $N_a(v)$ curves have maxima near -35 km s^{-1} and profile shapes that more closely resemble each other and the N V profile than they do the Al III profile. However, some of the Al III structure is related to higher ionization gas traced by Si IV and C IV. The Si IV and C IV profile asymmetries suggest the presence of absorption components near -34, -17, and $+6$ km s^{-1}. An additional asymmetry in the negative velocity wing of the C IV lines indicates the existence of a component near -68 km s^{-1}, which may be related to circumstellar material as discussed in § 4. The Al III profile asymmetries suggest the presence of broad components near -35 and $+10$ km s^{-1} and a narrow strong component near -15 km s^{-1}. The low ionization line of P II bears little resemblance to the highly ionized gas lines and obviously traces a very different gas distribution.

One can consider the effects of the varying ISF in interpreting profile similarities and differences in the data shown in

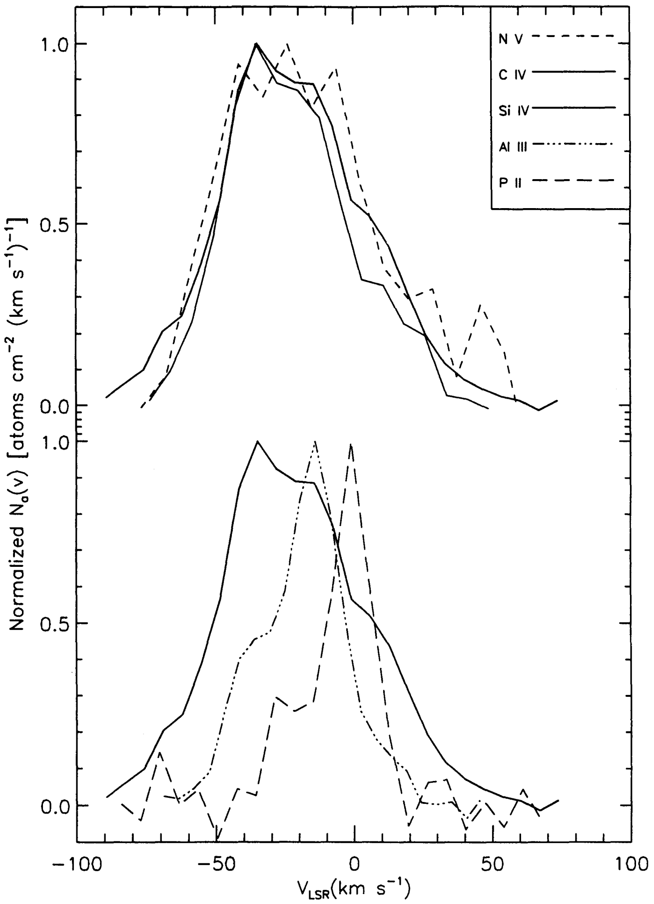

FIG. 5.—Apparent column density profile comparisons. We normalized the apparent column density profiles shown in Fig. 4 to unity at their peak values to produce this plot. *Top*: Note that the lines of Si IV, C IV, and N V have the same general appearance, although the C IV profile is noticeably broader than the Si IV profile. The slight enhancement near −35 km s^{-1} in the Si IV and C IV profiles may be due to Norma spiral arm gas at $z \approx -1$ kpc. *Bottom*: Note the different velocities and widths of the P II, Al III, and C IV lines illustrated. The profile differences are due largely to gas scale height and velocity dispersion differences in the distributions of the three ions. The strong central component in the Al III profile near −15 km s^{-1} is probably associated with gas in the Sagittarius-Carina spiral arm link and accounts for approximately 25% of the Al III along the sight line. The main P II concentration near 0 km s^{-1} arises in disk gas ($|z| < 200$ pc). C IV exhibits absorption out to large negative velocities due to its extended distribution and large gas velocity dispersion.

Figure 5. The ISF increases in breadth with decreasing wavelength and is therefore broadest at the wavelength of N V and narrowest at the wavelength of Al III. However, differences in the ISF for the various profiles cannot account for the profound differences seen in Figure 5. For example, degrading the Al III profile to the resolution of the high ion profiles weakens the peak absorption near −15 km s^{-1} but does little to change the rapid decreases in Al III at large velocities since the ISF width is small compared to the overall Al III profile widths. Differences of a few km s^{-1} in the ISF width for high ion lines as broad as those shown in Figures 1 and 4 have little impact on the observed shapes of the $N_a(v)$ profiles.

We plot ionic column density ratios as a function of LSR velocity in the panels of Figure 6. The following four ratios are illustrated: N(Si IV)/N(Al III), N(C IV)/N(Al III), N(C IV)/N(Si IV), and N(C IV)/N(N V). The solid vertical lines on each plot represent the $\pm 1\ \sigma$ errors carried through from Figure 4 added in quadrature with the error that results from a relative line shift of ± 3 km s^{-1}. The error in the ratio introduced from a ± 3 km s^{-1} shift of one profile relative to the other is comparable to or less than the error expected from statistical and continuum fitting uncertainties at velocities where the line

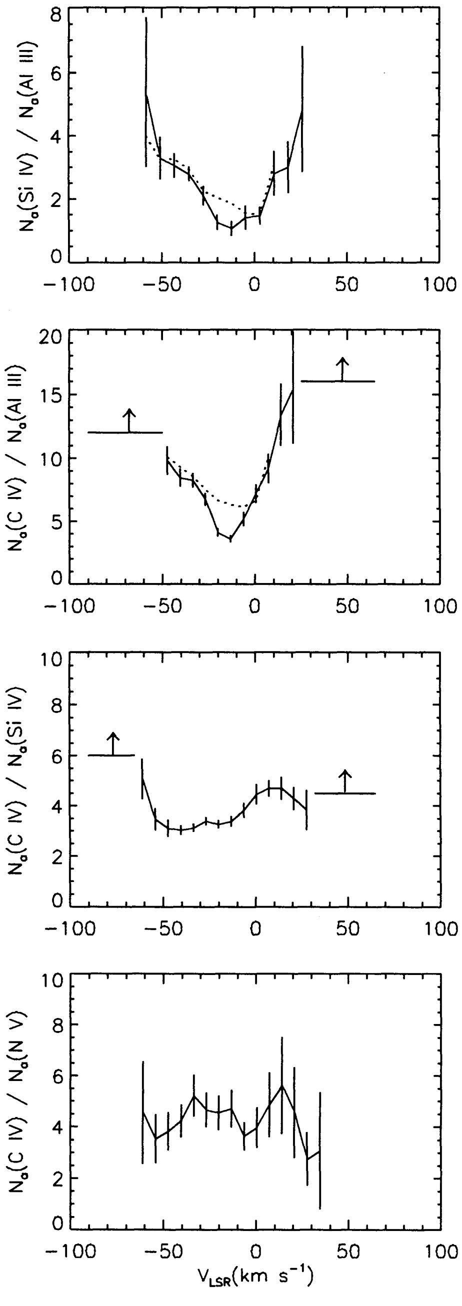

FIG. 6.—Ionic column density versus LSR velocity. We illustrate the following ratios: N(Si IV)/N(Al III), N(C IV)/N(Al III), N(C IV)/N(Si IV), and N(C IV)/N(N V). The 1 σ errors indicated by the solid vertical lines are due to continuum placement uncertainties, statistical noise fluctuations, and errors resulting from a ± 3 km s^{-1} velocity shift between individual species. When appropriate, lower limits for the ratio values are shown as solid lines with attached upward arrows. Dotted lines in the panels involving Al III indicate ratio values for the broad, turbulent Al III component (see text) after the absorption due to the strong narrow Al III component near −15 km s^{-1} is removed.

1994ApJ...431..201S

intensity is not changing rapidly, but it contributes significantly at those velocities where the derivative of the absorption profile is large. We discuss these ratios in § 7.

6. GAS KINEMATICS

The profiles shown in Figures 4 and 5 are kinematically complex and have shapes governed by a variety of factors that differ from species to species: the gas velocity dispersion, the stratification of the gas perpendicular to the Galactic plane, and the influence of large scale Galactic structures. Other factors contributing to the profile shapes include, but are not limited to, the ionization level of gas and gas phase depletion patterns at different locations along the sight line. We address the first set of factors in this section and the second set in § 7.

6.1. *Model Profiles*

We use a simple computer model of the halo gas distribution to predict the observed column density profiles of various species. The model predicts the column density per unit velocity by summing the column density contributions to each velocity interval at each distance interval along the sight line. We assume that the gas distribution is smoothly varying out to the distance of the star and has an exponential scale height, *H*. The remaining free parameters in the model are a mid-plane density, n_0, and a (constant) gas velocity dispersion expressed as a Doppler width, b_g. We use the Galactic rotation curve derived by Clemens (1985) for the relationship between gas velocity and distance along the sight line. General characteristics of the model and its use are fully described by Savage, Massa, & Sembach (1990).

To investigate the behavior of the individual parameters on the column density profile expected for the sight line, in Figure 7 we show the profiles calculated for a range of velocity dispersions (b_g = 10, 15, 20, 25, and 30 km s^{-1}), scale heights (H = 0.1, 0.3, 0.5, 1.0, and 3.0 kpc), and stellar distances (d = 3.0, 4.0, 5.0, and 6.0 kpc). Unless varied, the model parameters are $n_0 = 10^{-8}$ cm^{-3}, H = 1.0 kpc, b_g = 15 km s^{-1}, and d = 4.8 kpc. Increasing the distance of the star or scale height of the gas leads to larger amounts of absorption at negative velocities. Larger velocity dispersions lead to smoother $N(v)$ profiles. Note that the profile for b_g = 10 km s^{-1} has a twin peak due to gas bunching in velocity space along the sight line. The velocities of these peaks depend upon the remaining free parameters. For larger distances or scale heights, the blue peak is more pronounced and shifts to more negative velocities (i.e., more gas exists at distances closer to the sight line tangent point, d_{tp} = 5.1 kpc). None of the observed profiles show this double peaked behavior, which indicates that the either the observed species have larger velocity dispersions (Si IV, C IV,

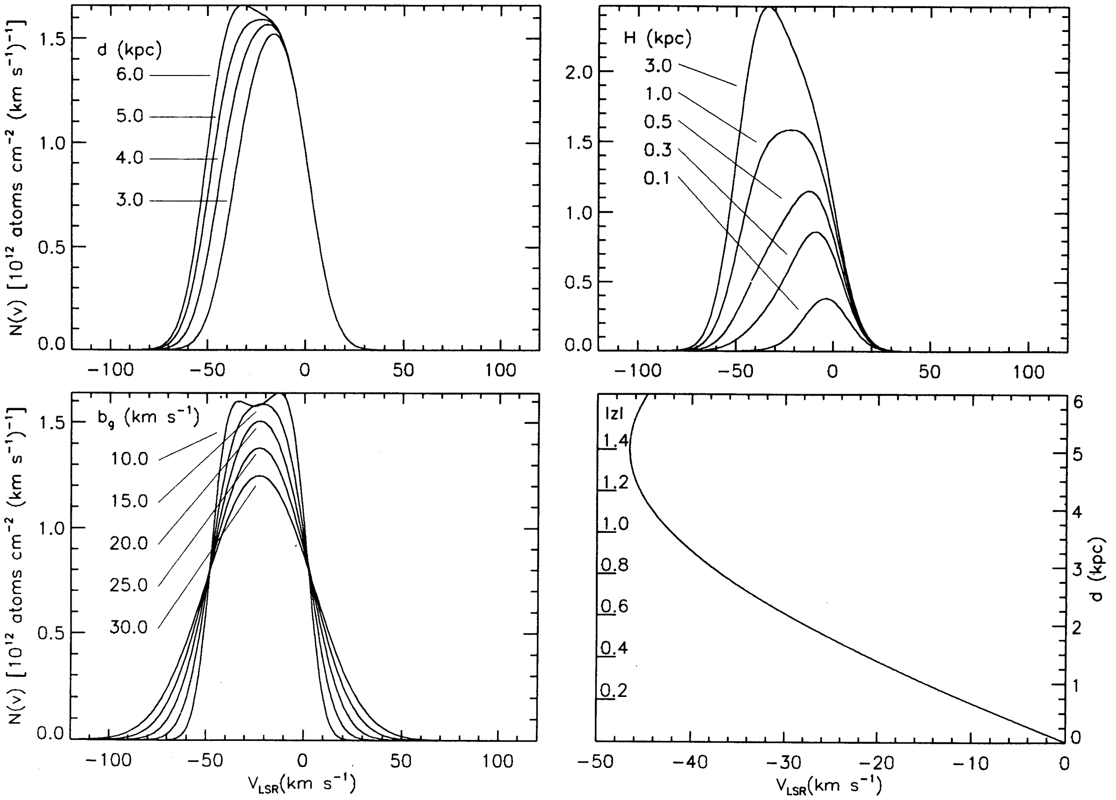

FIG. 7.—Model column density profiles as a function of LSR velocity for the HD 116852 sight line. All model profiles assume the gas has a constant velocity dispersion along the sight line, b_g, and an exponential density distribution perpendicular to the Galactic disk characterized by a mid-plane density, n_0, and a scale height, H. Unless otherwise indicated, $n_0 = 10^{-8}$ cm^{-3}, H = 1.0 kpc, b_g = 15 km s^{-1}, and d = 4.8 kpc. No instrumental spread function has been applied to the curves shown in this figure. In the lower right-hand panel, we show the expected relationship between LSR velocity and distance for this sight line using the Galactic rotation curve derived by Clemens (1985). The most negative velocity, v_{LSR} = −47 km s^{-1}, expected for the HD 116852 sight line occurs at a tangent point distance d_{tp} = 5.1 kpc, which occurs beyond the stellar distance of 4.8 kpc. These model results indicate that the following conditions must be satisfied for substantial quantities of gas to be seen at large negative velocities ($v_{LSR} < -50$ km s^{-1}: (1) a large stellar distance, $d > 4$ kpc, (2) a large scale height, $H \geq 1$ kpc, and (3) a large velocity dispersion, $b_g > 10$ km s^{-1}.

N V) or smaller scale heights (P II, Ge II, Al III). Although not illustrated, adjusting the mid-plane density of the gas, n_0, in the model results in a simple vertical scaling of the column density profiles. We have not convolved the instrumental spread function with the profiles shown in Figure 7.

In Figure 7 we also show the predicted velocities for corotating gas at various line-of-sight and vertical distances. Velocities out to -47 km s^{-1} are expected for $d < 6.0$ kpc. At distances greater than the distance of the sight line tangent point the expected velocity increases positively. To accumulate substantial column densities at large negative velocities, say $N_a(v) \sim 0.5\ N_a(v)_{\rm max}$, requires that two or more of the following conditions be satisfied: (1) the gas must have a substantial velocity dispersion, $b_g \geq 15$ km s^{-1}, (2) the gas must have a large scale height, $h \geq 1$ kpc, or (3) the sight line must be extended, $d \geq 4.0$ kpc. The positive velocity wing of the profile, which is not influenced by Galactic rotation, provides direct information about the velocity dispersion of the local gas.

We ignore the effects of noncorotating gas along the sight line. By "corotation" we mean that the Galactocentric rotational motion of the gas is independent of z. At very large z-distances, Galactic fountain models predict radial inflowing and/or outflowing motions that could be interpreted as deviations from corotation because they do not obey the general Galactic rotation law [i.e., $v = v(|z|)$ for R = constant]. Yet, corotating halo gas parcels could have additional motions in the z-direction that do not qualify as deviations from corotation. For the direction to HD 116852, the line-of-sight component of z-motions for corotating halo gas is reduced by a factor of $\sin|b| = 0.28$. Therefore, z-motions of the halo gas in this direction should not strongly influence the observed line profiles.

Lockman (1984) showed that the extended H I layer in the Galaxy between $R = 4$ and 8 kpc is corotating up to z-distances of 1 kpc. We believe a similar result holds for the highly ionized counterpart of this gas even though kinematical modeling of the high ion profiles of two inner Galaxy stars, HD 163522 and HD 156359 (Savage, Massa, & Sembach 1990; Sembach, Savage, & Massa 1991), has shown that there is a strong indication that halo gas in the inner Galaxy decouples from, and begins to lag behind, the underlying disk gas. Besides being at a z-distance less than the altitude at which these deviations from corotation were found to begin, the HD 116852 sight line never passes nearer than 7.0 kpc from the Galactic center (assuming a solar Galactocentric radius of 8.5 kpc), whereas the HD 156359 and HD 163522 sight lines pass within ~ 4 kpc of it. The observed profiles for the HD 116852 sight line are consistent with halo gas corotating up to the z-distance of the star, which is in qualitative agreement with the predictions by Sembach et al. (1991) that the altitude at which deviations from corotation set in is large, $|z| \geq 1.5$ kpc, and depends on Galactocentric radius. This result is also consistent with the simple model results presented by York et al. (1982) for the Mrk 509 sight line, which passes no closer than ~ 5 kpc from the Galactic center and has profile widths consistent with corotation up to large altitudes.

Additional variations such as changing the assumed shape of the Galactic rotation curve, the form of the density distribution perpendicular to the Galactic plane, or allowing the velocity dispersion to change along the sight line, can be made in the model. To consider all the possible effects of these, and other, parameters is beyond the scope of this paper. However, we believe that most do not seriously influence the principal conclusions of this paper, and for this reason, we continue to discuss only the simplest model parameters presented above.

We determined the best fit model parameters for the P II, Ge II, Al III, Si IV, C IV, and N V profiles through a chi-squared minimization of the model profiles to the observed data. We used a gradient expansion algorithm to do the minimization and convolved all model profiles with the appropriate ISF (see Table 1) during the minimization process. We merged the observed $N_a(v)$-values for each species having multiple lines into a single $N_a(v)$ profile for the species. No averaging or interpolation was necessary. We applied a simple correction to the data points in the cores of the Si IV and C IV profiles before modeling them to account for the small amount of unresolved saturated structure in the lines. The correction consisted of increasing the weak line $N_a(v)$-values by an amount equal to the difference in the $N_a(v)$-values for the weak and strong lines. This is a first-order approximation to the true Si IV and C IV $N_a(v)$ profiles and is based upon previous experience with lines of the same species having $f\lambda$ ratios of 2:1 (see Fig. 4 and Table 4 in Savage & Sembach 1991). For N V, we modeled only the λ1238 $N_a(v)$-values because the λ1242 $N_a(v)$ profile is subject to large continuum placement errors. We list the best-fit values and errors resulting from the fitting process in Table 4 along with the velocity ranges over which the minimization was performed. The best-fit model profiles are shown as solid lines in Figure 8 along with the observed values of $N_a(v)$, which are plotted as they are in Figure 4. Asterisks (*) identify the corrected Si IV and C IV $N_a(v)$-values. We ran two models for the Al III profiles, one to include and one to exclude the 0 to $+30$ km s^{-1} region of the profile spanning the strong narrow component centered on -15 km s^{-1}. Results from both Al III fits are listed in Table 4 and are shown as solid and dashed lines in Figure 8 for the inclusive and exclusive cases, respectively.

Errors due to continuum placement uncertainties and statistical noise fluctuations on individual points were formally propagated through the minimization process. A discussion of the errors associated with $N_a(v)$ profiles has been given by Sembach & Savage (1992). For a review of the methods for propagating errors through minimization processes, we recommend Bevington (1969) and Press et al. (1986). An important caveat applies when considering the errors listed in Table 4. These errors are appropriate for the assumed functional form and free parameters of the gas distribution. Alone they do not necessarily give a good indication of the overall quality of the fit to the data. For this reason, we list the χ^2_ν statistic for each of the fits. In several cases, the value of χ^2_ν is greater than unity, indicating that the assumed functional form and free parameters of the gas distribution are not entirely adequate in approximating the shape of the observed profiles. The true errors on the individual parameters in these cases may be larger than those listed in Table 4. In particular, the large Si IV and C IV χ^2_ν-values result mainly from the additional absorption present in the profiles near -35 km s^{-1} and $+20$ km s^{-1}. We discuss the effects of the additional absorption on measurable quantities, such as velocity dispersions, further in §§ 6.2 and 6.4.

The values of H listed for the high ions in Table 4 may be more poorly determined than the formal fitting errors suggest because the column density per unit velocity dependence upon mid-plane density, scale height, and velocity dispersion becomes subtle as H becomes comparable to the height of the star above the disk. As a result, the quantity $n_0 H$, which is better determined than either n_0 or H alone, may be somewhat

TABLE 4

BEST-FIT MODEL PARAMETERS FOR AN EXPONENTIAL GAS DISTRIBUTION[a]

Ion	n_0 (cm^{-3})	H (kpc)	b_g (km s^{-1})	log $N_{\rm model}$ (cm^{-2})	Range (km s^{-1})	χ_ν^2
P II	1.9 ± 0.6 (−7)	0.06 ± 0.02	7.1 ± 2.0	14.12 ± 0.20	[−150, 150]	1.15
Ge II	9.3 ± 2.8 (−10)	0.13 ± 0.04	6.2 ± 3.7	12.13 ± 0.20	[−150, 150]	0.89
Al III	3.2 ± 0.2 (−9)	0.56 ± 0.04[b]	11.6 ± 1.7	13.25 ± 0.04	[−150, 150]	3.83
Al III	2.2 ± 0.2 (−9)	0.73 ± 0.07[b]	14.1 ± 1.4	13.18 ± 0.06	[−150, −30]; [0, 150]	1.09
Si IV	3.5 ± 0.2 (−9)	2.2 ± 0.4[c]	15.4 ± 1.1	13.56 ± 0.09	[−150, 150]	7.27
C IV	1.5 ± 0.1 (−8)	1.17 ± 0.11[c]	28.6 ± 0.9	14.12 ± 0.06	[−150, 150]	5.98
N V	3.7 ± 0.6 (−9)	0.92 ± 0.28[c]	30.6 ± 3.5	13.46 ± 0.18	[−150, 150]	1.10

[a] Results of the model profile fitting discussed in § 6.1. The large values of χ_ν^2 in some cases indicate that the model does not reproduce the entire velocity distribution of the observed profiles well.

[b] The two scale heights listed for Al III include and exclude the effects of the narrow Al III absorption component centered near −15 km s^{-1}.

[c] Since HD 116852 is situated in the low halo at $z = -1.3$ kpc, the models do not strongly constrain scale height values exceeding ≈1 kpc. The large values of χ_ν^2 for Si IV and C IV reveal that the detailed structure in the observed profiles is not adequately described by the simple model described in the text (see Fig. 8).

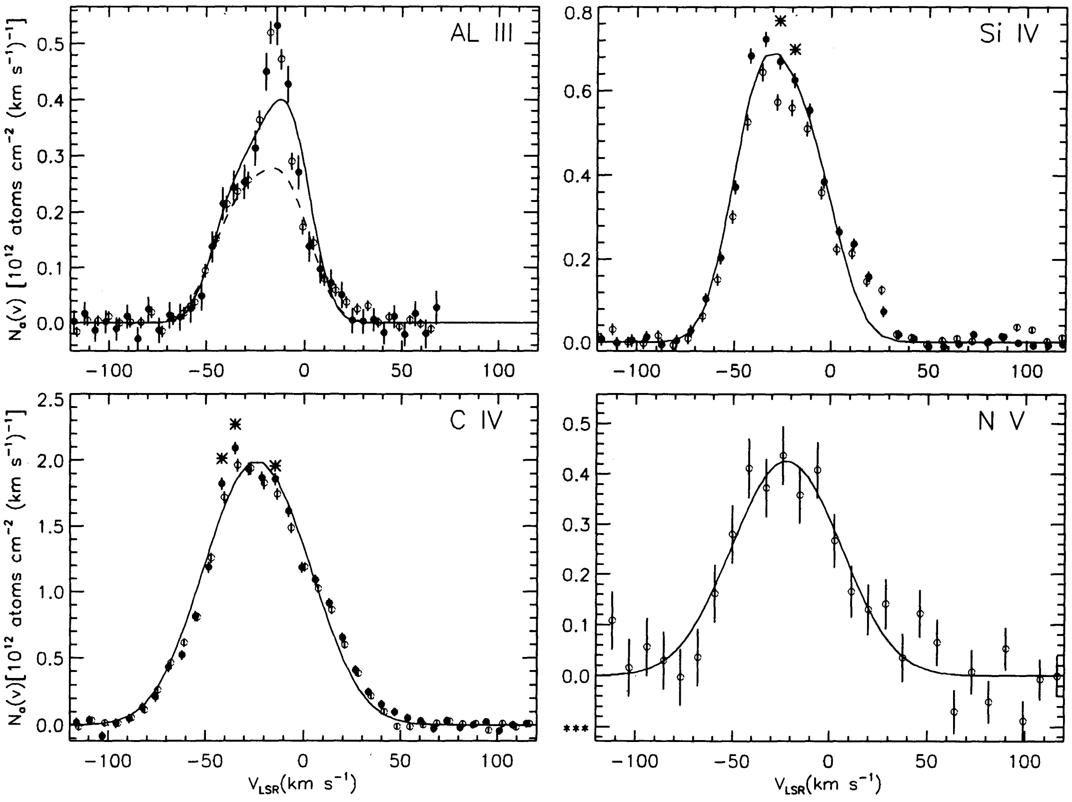

FIG. 8.—Apparent column density profiles and best-fit model profiles vs. LSR velocity. Filled and open circles represent values of $N_a(v)$ [atoms cm^{-2} (km s^{-1})$^{-1}$] for the weak and strong member of each doublet, respectively. The solid lines indicate $N_a(v)$-values for the best-fit model results listed in Table 4. The model results account for the ISF of the GHRS observations. Before fitting the Si IV and C IV lines, we corrected the data values in the core affected by unresolved saturated structure according to the method outlined in § 5.1. These corrected values of $N_a(v)$ are indicated by asterisks (*). We ran two models for Al III. The solid line indicates values for the model fit over the entire observed profile. The dashed line indicates values for the model fit over the observed Al III profiles excluding the range from 0 to +40 km s^{-1}. Note that both Al III models underestimate the amount of material near the peak of the $N_a(v)$ profile. For Si IV and C IV, the model profiles underestimate the amount of material near −35 km s^{-1} and at positive velocities. We discuss the quality of the fits to the observed profiles in § 6.1 and list their values of χ_ν^2 in Table 4.

smaller for the high ions toward HD 116852 than for a sight line penetrating through the entire halo because substantial quantities of highly ionized gas are known to exist at $|z| \geq 1.3$ kpc.

In Table 4 we also list the integrated column density of the best-fit model for comparison with the observed values. In all but one case, that of the modified Al III profile where the -15 km s^{-1} absorption component is ignored, the model integrated column densities are in reasonable agreement with the observed values. The model profiles shown in Figure 7 for Si IV, C IV, and N V reproduce the general character of the observed absorption well, but cannot reproduce all the observed line inflections for each ion.

6.2. *Velocity Dispersions*

In our analysis we have adopted a single value of the gas velocity dispersion, b_g, along the sight line for each species.[5] The gas velocity dispersion probably changes as a function of R (or d or z), but we are unable to justify incorporating a changing velocity dispersion into our model without additional information about the functional form of such changes. We are therefore left to consider the "average" values for the entire profiles like those listed in Table 4 or values derived from portions of the profiles dominated by dispersion effects. One such possibility for isolating velocity dispersion effects on the profile shapes is to examine only the absorption occurring at positive gas velocities. We do not expect positive gas velocities for corotating material along the HD 116852 sight line for $d < 10$ kpc (see lower right panel of Fig. 7). Therefore, any absorption observed at positive ("forbidden") velocities probably is due to the intrinsic velocity dispersion of the gas. For a large number of components distributed along the sight line, one can think of this dispersion as a cloud-to-cloud velocity dispersion of relatively nearby disk gas.

We define the velocity dispersion in the positive velocity gas by

$$b_g(v \geq 0) = \sqrt{2}\left(\frac{\int N_a(v) v^2\, dv}{\int N_a(v)\, dv}\right)^{1/2} \quad \text{for} \quad v > 0\,. \qquad (3)$$

For a Gaussian distribution centered at zero velocity, $b_g(v \geq 0) = \sqrt{2}\,\sigma$, where σ is the typical Gaussian profile dispersion. This definition allows us to calculate a value for the profile weighted width of the line at positive velocities without assuming a particular functional form for the distribution. We list the values of $b_g(v \geq 0)$ for low-ionization (Na I, Mg II, P II, Ca II, Ge II), intermediate-ionization (Al III), and high-ionization (Si IV, C IV, and N V) species in Table 5. Note that accurate measures of $b_g(v \geq 0)$ can be derived for species containing substantial saturated structure in the line cores, like Na I, since the optical depths of the lines are generally small for $v > 0$ km s^{-1}. Table 5 contains $\pm 1\,\sigma$ errors derived by propagating the errors on $N_a(v)$ through equation (3). The errors also allow for a 3 km s^{-1} zero velocity offset uncertainty in the $N_a(v)$ profiles. The definition of $b_g(v \geq 0)$ is most appropriate for those lines (i.e., Si IV, C IV, N V) where the positive velocity extents of the profiles are large compared to the instrumental widths. For weaker lines of the neutral species such as Ge II or P II, for which this may not be the case, the values of $b_g(v \geq 0)$ reflect contributions from both the intrinsic line widths and the instrumental line width through the convolution present in the definition of $N_a(v)$.

TABLE 5

GAS VELOCITY DISPERSIONS (km s^{-1})[a]

Species	HD 116852	HD 167756
Na I	8.2 ± 0.3	11.2 ± 0.3
Ca II	13.4 ± 0.8	24.2 ± 0.4
Mg II[b]	6.8 ± 5.7	10.6 ± 1.6
Ge II	17.8 ± 7.3	...
P II	13.6 ± 5.8	...
Al III	19.0 ± 3.7	...
Si IV	23.3 ± 2.3	37.2 ± 2.0
C IV	27.3 ± 2.1	37.8 ± 1.6
N V	30.7 ± 5.5	38.3 ± 3.0

[a] Velocity dispersions, $b_g(v \geq 0) = [2\langle(v \geq 0)^2\rangle]^{1/2}$ in km s^{-1} calculated by direct integration of the profiles at positive velocities unaffected by Galactic rotation. The HD 167756 dispersions were calculated using the GHRS echelle data presented by Savage et al. 1994. The positive velocity extension of the profile integrations for deriving $b_g(v \geq 0)$ is similar to that used for the equivalent width integrations (see Table 1).

[b] The HD 116852 Mg II data is affected by unresolved saturated structure at positive velocities.

[c] Instrumental line widths have not been accounted for in listed values, but any contributions appear to be small based upon an analysis of smoothed and unsmoothed versions of the HD 167756 data.

For the HD 116852 sight line we find $b_g(v \geq 0) = 19.0 \pm 3.7$, 23.3 ± 2.3, 27.3 ± 2.1, and 30.7 ± 5.5 km s^{-1} for Al III, Si IV, C IV, and N V. The values of $b_g(v \geq 0)$ represent independent measures of the gas phase velocity dispersions traced by these ions and reveal important differences between the different ionization stages of the gas. There is a clear trend for increasing velocity dispersion as a function of the ionization level of the species being probed. The global profile fits listed in Table 4 also reflect this trend, but by isolating only the positive velocity gas we have assured that velocity dispersion effects are the dominant contributor to the profile shapes. The larger values of $b_g(v \geq 0)$ in Table 5 compared to b_g calculated from the model profiles in the previous section (see Table 4) result from more complete estimations of the positive velocity absorption by $b_g(v \geq 0)$. This is particularly relevant for the Si IV and C IV lines, since the model fits in § 6.1 underestimate the absorption at positive velocities (Fig. 8).

The large dispersions observed for the ionized gas cannot be due solely to a single thermally broadened component because the inferred temperatures, $T = (0.5\text{–}1.0) \times 10^6$ K, are many times larger than the temperatures at which Al III, Si IV, C IV, and N V peak in abundance under equilibrium situations where collisional ionizations balance recombinations (Sutherland & Dopita 1993). Trace amounts of the ions are expected in gases at these temperatures, and nonequilibrium effects resulting from the short cooling times of the ions lead to lower gas temperatures than expected under equilibrium conditions, thereby further weakening the likelihood of a single component interpretation. The large single component temperatures, which are also inconsistent with the observed column density ratios of the ions (§ 7), and the inflections and apparent structure within the lines (§ 5.2) lead us to conclude that some contribution to the values of b_g must result from a combination of thermal line broadening and the superposition of individual cloud-to-cloud motions along the sight line.

---

[5] Note that the dispersion values listed by various authors are often given as a formal dispersion, σ, which is related to b_g through $b_g = \sqrt{2}\,\sigma$. All dispersions listed in this paper are expressed in terms of b_g.

1994ApJ...431..201S

In the diffuse ionized gas traced by Galactic Hα emission, Reynolds (1985, 1993) finds average velocity dispersions of 12 to 30 km s^{-1} resulting from nonthermal random motions and differential Galactic rotation. Most of the hydrogen is ionized in the diffuse Hα emitting gas, $n(\text{H II})/n(\text{H I}) > 15$ if $T_e \approx 8000$ K (Reynolds 1993). The velocity dispersion we find for Al III is similar to the values on the lower end of the Hα dispersion distribution, but the larger dispersions we find for Si IV, C IV, and N V cannot be attributed to this gas since the values of $b_g(v \geq 0)$ measure the dispersion in gas that is unaffected by differential Galactic rotation effects. Therefore, the relationship of the ionized gas seen along the HD 116852 sight line and the diffuse Hα background is uncertain at present, but it at least seems plausible that some of the Al III absorption and diffuse Hα emission in the Galaxy may be related given their similar velocity dispersions and vertical distributions (see § 6.3).

The trend for increasing values of $b_g(v \geq 0)$ with increasing ionization is not unique to the HD 116852 sight line; similarly impressive relationships exist for the high-latitude sight lines toward HD 18100 and HD 100340 where a large range in the ionization level of the gas is observed (Savage & Sembach 1994). In a detailed study of 12 halo sight lines, Sembach & Savage (1992) found that differences in the velocity dispersions of the ionized gas lines cannot be due to thermal width differences alone and must be the result of turbulent or flowing gas motions. For example, the large velocity dispersions found for the high ion lines toward HD 167756 are associated with a high temperature ($T \sim 2$–8×10^5 K) gas that is widely distributed and may arise in over-pressurized ($p/k \sim 2.4 \times 10^4 f^{-1}$ atoms cm^{-3}) Galactic worm or supershell structures along the sight line (Savage et al. 1994). In Table 5 we list the values of $b_g(v \geq 0)$ for the HD 167756 sight line we derive from GHRS echelle data together with the HD 116852 values. (For lines as broad as the HD 167756 high ion lines, the differences between the dispersions derived at echelle resolution and those derived at the resolution of the G160M grating used in this study are minimal). We compare the HD 116852 and HD 167756 results in Figure 9, where we plot the values of $b_g(v \geq 0)$ as a function of ionization potential. For both sight lines a trend for increasing velocity dispersion with increasing ionization level is readily apparent. The high ion velocity dispersions for the HD 116852 sight line are about 10 km s^{-1} smaller than those for HD 167756, but the low ion (Na I, Mg II) separations are considerably smaller. However, note that the Ca II difference is comparable to the high ion differences, perhaps as the result of enhanced grain destruction along the HD 167756 sight line. The HD 167756 high ion dispersions are typical of those found for other Galactic center sight lines (see Savage et al. 1990; Sembach et al. 1991), indicating that ionized gas along the interarm direction toward HD 116852 is more quiescent, or perhaps less ionized, than gas along comparable path lengths toward the Galactic center.

Differences in the low and high ion velocity dispersions argue against the coexistence of the two types of species in the same gas. The low ionization species listed in Table 5 have $b_g(v \geq 0) \leq 15$ km s^{-1}, while the higher ions have $b_g(v \geq 0) \approx$

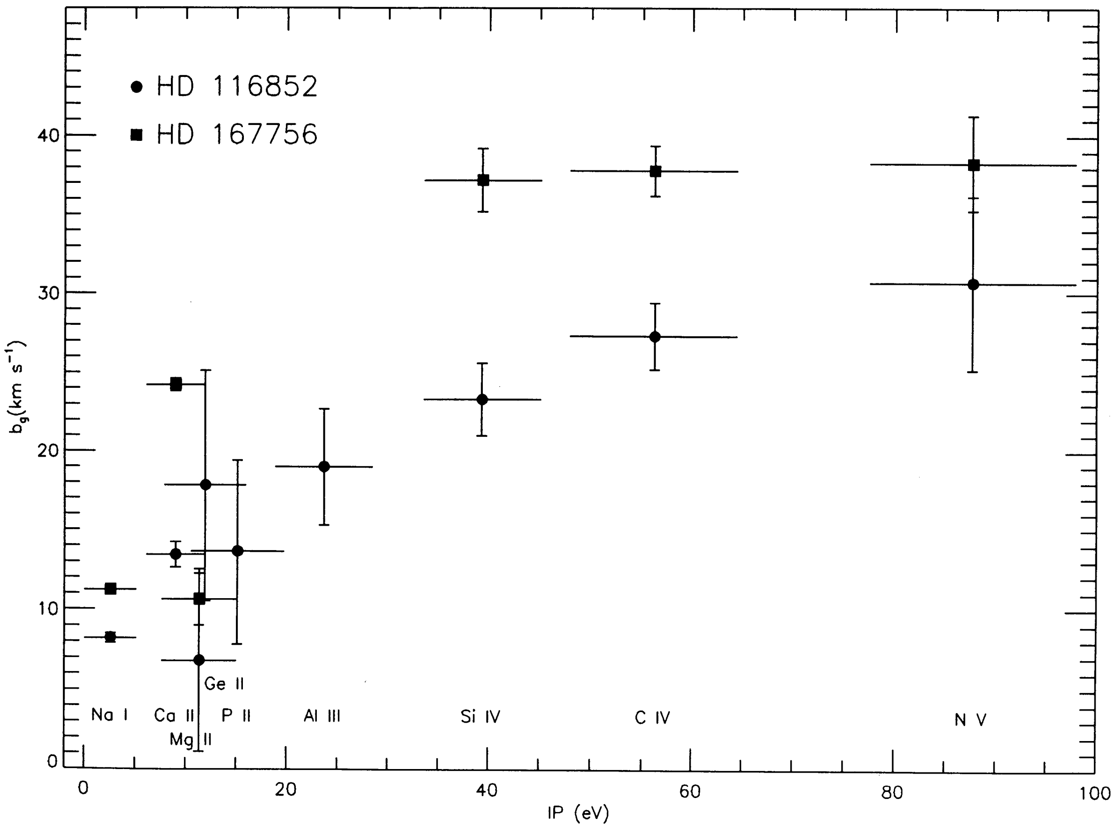

FIG. 9.—Velocity dispersion, $b_g(v \geq 0)$, vs. ionization potential for the interstellar lines observed toward HD 116852 and HD 167756. The values of $b_g(v \geq 0)$ are those from the positive velocity portions of the profiles, which are unaffected by differential Galactic rotation. The vertical error bars represent $\pm 1\ \sigma$ errors due to continuum placement and statistical uncertainties. The horizontal error bars indicate the energy ranges for each species specified at the bottom of the plot.

25 to 30 km s^{-1}. If the two types of gas are spatially related [for example, in evaporative fronts between warm clouds and a hot surrounding medium of the type postulated by McKee & Ostriker (1977)], then portions of the neutral and weakly ionized gas may be associated with a higher velocity dispersion phase like that seen in H I 21 cm emission (Kulkarni & Fich 1985) or Ca II absorption toward distant stars (Sembach & Danks 1994). Flow velocities in plane parallel fronts are adequate to explain the observed differences in the low and high ion dispersions (R. Benjamin 1993, private communication).

6.3. *Scale Heights*

The gas scale heights, *H*, we find from the apparent column density profile fitting in § 6.1 are substantially larger for Si IV, C IV, and N V ($H \geq 1$ kpc) than they are for lower ionization species like P II or Ge II ($H \leq 0.2$ kpc) (see Table 4). The Al III scale height of 0.6 to 0.7 kpc represents an intermediate case and supports the conclusion that the scale height of the gas depends upon its ionization state. The effects of the scale height differences on the observed profile shapes are clearly visible in Figures 1, 4, 5, and 8. The increasing strength of the high ion profiles with increasingly negative velocities is a common feature of profiles for an extended gas distribution with a moderate velocity dispersion. Highly ionized gas exists up to several kpc from the Galactic plane (Savage & Massa 1987; Sembach & Savage 1992), and the high ion profiles toward HD 116852 are consistent with this result. The low ion scale heights are in accord with those found for neutral hydrogen in the Galaxy (Lockman 1984). If we attribute the negative velocity extents of the Ni II and Ca II profiles shown in Figure 1 to differential Galactic rotation, then absorption by these species in low ion velocity interval III (i.e., $v < -35$ km s^{-1}) occurs in gas at distances of more than 750 pc below the Galactic plane. The large negative velocity extents of the refractory element profiles may be due to the return of these species into the gas phase at large *z*-distances by shock destruction of grains (Edgar & Savage 1989). Since typical depletions for the refractory elements range from a factor of 10 to 100 below solar values in the diffuse interstellar medium of the Galactic disk (Jenkins 1987), small amounts of grain destruction lead to large increases in the gas phase abundances of these elements. Elements such as sodium, phosphorous, and sulfur, which exist largely in the gas phase, show no large increases in absorption strength in velocity interval III relative to the zero velocity (interval I) strength.

Highly ionized gas at large *z*-distances provides a diagnostic probe of the gas energetics and kinematics in the Galaxy. Much of the highly ionized gas appears to result from energetic events in the Galactic disk, such as supernovae explosions, that shock heat the surrounding disk gas and expel it into the halo. Once the heated gas escapes from the plane into the halo, it cools and recombines to form detectable species such as Si IV, C IV, and N V. Models of the gas ionization in simple Galactic fountain situations predict average high ion column density ratios similar to those shown in Figure 6 (Shapiro & Benjamin 1993), but the general inability of such models to predict the shapes of the line profiles and account for complicated geometries remains a weakness.

The Al III scale height of 0.6 to 0.7 kpc for the HD 116852 sight line agrees reasonably well with the average value of 1 kpc found by Savage et al. (1989) for Al III along 31 low-density sight lines in the Galaxy and by Savage et al. (1990) in a detailed study of the inner Galaxy sight line toward HD 163522. The diffuse ionized media in the Milky Way (Reynolds 1993) and external galaxies like NGC 891 (Dettmar 1990) traced by Hα emission measurements have similar vertical distributions. The deficiency of Al III at large *z*-distances (i.e., $|z| > 1$ kpc) supports the hypothesis that large amounts of Al III are not produced in a circulating fountain until the recombining gas begins to re-enter the domain of the thick Galactic gaseous disk ($|z| \leq 1$ kpc). Al III produced in cooling gas exists over a narrow temperature range, $T \sim 2\text{–}5 \times 10^4$ K (Hartquist, Snijders, & West 1983), and should be found at lower $|z|$ than more highly ionized species like Si IV, C IV, and N V that survive at higher temperatures. However, the scale height of Al III is also consistent with creation in a lower temperature Galactic fountain than the one normally invoked to explain the large vertical extent of the highly ionized gas ($T_{\rm initial} \sim 10^5$ K vs. $T_{\rm initial} \sim 10^6$ K; Houck & Bregman 1990). Low temperature Galactic fountains can also qualitatively explain the infalling motions of high-velocity clouds, HVCs, identified in neutral species toward high Galactic latitudes (Wakker 1991), although the existence of HVCs in the halo at substantial *z*-distances has not yet been convincingly demonstrated (but see Danly, Albert, & Kuntz 1993 for an interesting recent HVC distance determination).

6.4. *Links to Large-Scale Structure*

There is evidence in the observed profiles that some of the ionized gas absorption is associated with large-scale Galactic structure along the sight line. In particular, the significant enhancement near -15 km s^{-1} in the Al III profiles has a velocity within a few km s^{-1} of gas located in the Carina link region of the Sagittarius spiral arm (see § 4.1). Both the velocity and lower sight line crossing of the Sagittarius arm make it a more tenable site for the enhanced Al III absorption than the Norma-Centaurus spiral arm ($z \approx -0.5$ kpc vs. $z \approx -1$ kpc). The -15 km s^{-1} Al III enhancement is probably the result of enhanced ionization rather than an increase in the gas phase aluminium abundance since lower ionization species, such as Ni II and Ca II, that have similar depletion patterns and vertical distributions show no such increase at -15 km s^{-1} relative to zero velocity absorption.

The weak enhancement in the Si IV and C IV profiles near -35 km s^{-1} may also be associated with a spiral arm. The Norma-Centaurus spiral feature contains gas with velocities between -30 and -50 km s^{-1} and is kinematically distinct from the Sagittarius arm (see § 4). The model results of § 6.1 show that a simple smoothly distributed gas layer underestimates the observed high ion absorption at these velocities (Fig. 8). There is no strong change in the high ion column density ratios at this velocity, but the *N*(C IV)/*N*(Si IV) ratio is lowest at these velocities and the *N*(C IV)/*N*(Al III) ratio has a plateau over this range. Both results favor the presence of ionized gas with a character different from the underlying distribution. If the absorption is associated with the Norma-Centaurus spiral arm, it is at large distances from the Galactic plane ($z \sim -1$ kpc).

With the exception of the two cases mentioned in this section, there is no indication of other-large scale structure contributions to the observed profiles. There is also no evidence of abrupt changes in the high ion distribution as a function of distance from the Galactic plane. This is important because some Galactic halo support and ionization models rely upon an extragalactic radiation field to provide the ionizing photons required to maintain highly ionized species at large z-distances (Hartquist, Pettini, & Tallant 1984; Chevalier & Fransson 1984). The absence of abrupt changes in the high ion column densities or ratios as a function of $|z|$ indicate that either the disk and low halo gases are well mixed or the mechanisms governing the production of these species are similar in the disk and low halo (Sembach & Savage 1992).

7. GAS IONIZATION

Answers to fundamental questions about the ionization mechanisms and physical conditions in the ionized interstellar medium can be addressed with data of the type obtained for this study. Absorption lines from a range of ionization states spanning 100 eV (Na I to N V; see Table 2) are shown in Figure 1. In this section, we discuss the ionization processes affecting Al III, Si IV, C IV, and N V.

7.1. *Moderately Ionized Gas:* Al III *Absorption*

The Al III absorption profiles for the HD 116852 sight line consist of a strong narrow component near -15 km s^{-1} and a broad underlying distribution that probably results from the superposition of multiple weaker components. These two types of Al III absorption are clearly visible in the apparent column density profiles shown in Figures 4 and 8.

A fit to the narrow Al III component near -15 km s^{-1} after removing the broader Al III distribution modeled in § 6 yields $\langle v \rangle = -15.3$, $b = 4.7$, and log N(Al III) = 12.64. Although this component is much more pronounced in the Al III profiles than it is in the higher ion profiles, the Si IV and C IV lines do show evidence of an absorption feature near -15 km s^{-1}. The widths of the Al III and Si IV components should be similar if they arise in the same gas since the atomic weights of aluminium and silicon are similar. A single Gaussian component fit to the Si IV $N_a(v)$ profiles at -15 km s^{-1} with $b = 4.7$ km s^{-1} yields log N(Si IV) ≤ 12.76, which leads to N(Si IV)/N(Al III) ≤ 1.3. We find that the -15 km s^{-1} feature accounts for approximately 25% of the Al III along the sight line and as much as 17% of the Si IV.

The amount of Si IV relative to Al III in a plasma is given by N(Si IV)/N(Al III) = (Si/Al) [N(Si IV)/N(Si)] [N(Al)/N(Al III)]. In collisional ionization equilibrium a gas of solar composition, (Si/Al) = 11.75 (Anders & Grevesse 1989), has N(Si IV)/N(Al III) ≤ 1.3 for $T \leq 3.2 \times 10^4$ K (Sutherland & Dopita 1993). This temperature is consistent with the upper limit of $T = 3.4 \times 10^4$ K derived from the $b = 4.7$ km s^{-1} width of the component in the absence of turbulence. Due to the highly variable gas phase abundance of Si IV in nonequilibrium situations, our upper limit on the Si IV to Al III ratio does not place strong constraints on the temperature of the gas in a time-dependent isochorically or isobarically cooling gas [N(Si IV) changes by a factor of 1400 between 2.5×10^4 and 3.2×10^4 K under such conditions; R. J. Edgar 1993, private communication]. However, it is unlikely that $T < 2.0 \times 10^4$ K if the gas is collisionally ionized since the Al III fractional abundance drops rapidly at lower temperatures (Hartquist et al. 1983).

The width of the narrow Al III component is consistent with the widths of the diffuse photoionized gas seen in H II regions (Reynolds 1985, 1993) where turbulent motions often dominate the ionized gas line widths. For instance, the turbulent H II region surrounding ζ Oph has Al III and Si IV line widths comparable to the $b = 4.7$ km s^{-1} width we find for the -15 km s^{-1} feature. (Sembach et al. 1994). The -15 km s^{-1} Al III component also has a width very similar to those derived for the -16 km s^{-1} Na I and Ca II components along the HD 116852 sight line derived by Sembach et al. (1993). If the Al III and lower ionization species are tracing the same gas, then the component is indeed broadened by turbulent motions and the gas must have a temperature $T < 2.0 \times 10^4$ K.

The broad underlying distribution of Al III present in the profiles shown in Figure 4 has a cloud-to-cloud dispersion $b_g \approx 15$ to 20 km s^{-1}. The similarlity of the broad Al III and Si IV dispersions suggests that some of the absorption arising in the Al III and Si IV distributions are related. The Al III profiles reveal components at velocities where the higher ionization lines of Si IV and C IV show substructure; all three ions have line inflections near -35, -15, and $+10$ km s^{-1}. While the ion ratios shown in Figure 6 contain structure at the same velocities, the changes are minor in comparison to the general trends in the ratios. Between -50 km s^{-1} and $+20$ km s^{-1}, N(C IV)/N(Al III) = 3.8 to 16. Over the same range, N(Si IV)/N(Al III) = 2.1 to 3.5. Both ratios increase rapidly at larger positive and negative velocities. The lowest column density ratios occur at velocities near the strong, narrow Al III absorption at -15 km s^{-1}. In Figure 6, short dashed lines indicate the values of N(C IV)/N(Al III) and N(Si IV)/N(Al III) with the narrow -15 km s^{-1} component removed.

The evidence for a photoionized origin for the broad Al III component distribution is limited. Perhaps the most compelling reason to believe that some of the Al III is photoionized is the similarity of the inferred velocity distribution and scale height of the broad Al III distribution and the diffuse Hα emission observed by Reynolds (1993). One must take care in generalizing the Hα results to the HD 116852 sight line since the emission measurements were obtained for other directions. Yet, the zero order similarities are interesting and should be investigated further with measurements of these species along similar paths through the low halo. The main drawback to a photoionization origin is the general inability of Galactic photoionization models to produce highly ionized gas in appreciable quantities. Hot star photoionization models used to explain the diffuse ionized gas layer in the Galaxy produce small amounts of Si IV and C IV relative to species with ionization potentials similar to the Al III creation energy of 18.8 eV (see Evans & Dopita 1985; Sokolowski 1994). Models involving photoionization of low density halo gas by the extragalactic radiation field predict N(Si IV)/N(Al III) = 18 and N(C IV)/N(Al III) = 42 (Fransson & Chevalier 1985), in clear violation of the observed ratios for $-50 \leq v \leq +20$ km s^{-1} unless aluminum is depleted from the gas phase by a factor of 4 to 8 relative to carbon and silicon. Yet some dust destruction must be occurring at high $|z|$ to account for the enhanced Ca II and Ni II in at $v \leq -35$ km s^{-1} (velocity interval III; see Fig. 1). More importantly, the extragalactic photoionization models fail to reproduce the observed velocity structure of the absorption because they predict an abrupt increase in the amount of C IV and Si IV near $|z| \sim 1$ kpc, which corresponds to $v \approx -45$ km s^{-1} for the HD 116852 sight line.

Alternatively, the broad distribution Al III absorption components may arise in conductive interfaces or cooling collisionally ionized gas, where the Al III-bearing gas would have $T = 2\text{–}5 \times 10^4$ K. The amount of Si IV and C IV associated with the interfaces would depend strongly upon the temperature of the Si IV- and C IV-bearing gas. However, typical high ion column densities for interfaces of the type described by Borkowski, Balbus, & Fristrom (1990) are smaller than the total Si IV and C IV columns, which means that several interfaces or suitably inclined single interfaces are required to reproduce the observed columns.

7.2. *Highly Ionized Gas*: Si IV, C IV, *and* N V

Much, if not all, of the N V seen toward HD 116852 is created by collisional ionization in hot gas rather than by photoionization in warm gas because most hot stars have strong He II absorption edges, which greatly reduce the flux of 77 eV photons required to convert N IV into N V. The number of sources capable of providing photons with $E > 54$ eV is limited (Bregman & Harrington 1986), and observational detections of N V along other extended sight lines indicate that the observed N V columns are orders of magnitude greater than those expected from these sources (Sembach & Savage 1992). Si IV and C IV have ionization potentials at energies below the He II threshold and could, in principle, be produced partly by photoionization. Si IV, C IV, and N V peak in abundance in collisional ionization equilibrium at temperatures $T = 6.3 \times 10^4$, 1.0×10^5, and 1.8×10^5 K, respectively (Sutherland & Dopita 1993). Of the three ions, N V is the best temperature diagnostic because it is less affected by nonequilibrium effects than Si IV and C IV (see Fig. 17 of Sutherland and Dopita). Calculations of the time-dependent, nonequilibrium cooling of shock heated gas show that significant fractions of carbon and silicon can exist in the triply ionized state even at temperatures as low as 10^4 K (Shapiro & Moore 1976; Edgar & Chevalier 1986), but the column density ratios illustrated in Figure 6 best match those occurring in gases at larger temperatures, indicating that a substantial fraction of the high ion absorption is probably produced by collisional ionization in gas with $T \sim 10^5$ K rather than by photoionization in gas with $T \sim 10^4$ K.

The ratio of C IV to N V is approximately constant between -65 and $+40$ km s^{-1} and has a value of 4.3 ± 0.8. The constancy of the ratio implies that the processes governing the creation of these two ions are similar over this velocity range and probably results from collisional ionization of the gas at $T \approx 1.0 \times 10^5$ or $T \approx 3.2 \times 10^5$ K if the gas is in collisional ionization equilibrium. Note that non-equilibrium effects serve to increase this temperature since N(C IV) increases faster than N(N V) decreases as T decreases. Sembach & Savage (1992) reached a similar conclusion for a sample of twelve sight lines in the Galactic disk and halo having $\langle N$(C IV)/N(N V)$\rangle = 4.6 \pm 2.3$. Calculations of the amount of C IV relative to N V exist for a variety of astrophysical phenomena, such as supernova remnant bubbles (Weaver et al. 1977; Jenkins 1981; Slavin & Cox 1992, 1993) and Galactic fountains (Edgar & Chevalier 1986; Shapiro & Benjamin 1993) where cooling, hot gas is present. The cooling gas calculations generally predict time-averaged values of N(C IV)/N(N V) ≈ 1.5 to 3.6, although more detailed calculations involving magnetized conduction fronts at different evolutionary times (Borkowski et al. 1990) indicate that larger values of N(C IV)/N(N V) occur for fronts in very early ($< 10^5$ yr) stages of development.

The ratio of C IV to Si IV ranges from about 2.8 to 4.5 between -50 and $+30$ km s^{-1} and increases rapidly to values greater than 5.0 for velocities outside this range (Fig. 6). Theoretical predictions of the value of the N(C IV)/N(Si IV) ratio for cooling, hot gas situations is less certain than for the N(C IV)/N(N V) ratio, in large part because of the difficulties encountered in incorporating the ionizing effects of photons created within the cooling flow itself. The observed values of N(C IV)/N(Si IV) in the -50 km s^{-1} to $+30$ km s^{-1} range are similar to the integrated values for a sample of halo stars studied by Sembach & Savage (1992) who found $\langle N$(C IV)/N(Si IV)$\rangle = 3.6 \pm 1.3$. Most theoretical cooling gas calculations predict a ratio of 10 to 20 (see Table 10 of Sembach & Savage 1992), but models of one-dimensional, planar flows that account for self-photoionization in the flows (Shapiro & Benjamin 1993) predict C IV to Si IV ratios in general agreement with the observations.

The systematically decreasing value of N(C IV)/N(Si IV) from 0 to -40 km s^{-1} may provide significant new insight into the distribution of ionized gas along the sight line. Unfortunately, the larger errors on the N(C IV)/N(N V) ratio shown in Figure 6 do not allow us to conclude whether a similar trend exists for this ratio. These ratio changes are reflected in the relative scale heights of the three ions listed in Table 4. The Si IV scale height is a factor of 2 larger than the C IV and N V scale heights, and although our ability to discern differences in vertical distributions of species with scale heights near, or in excess of, the z-distance of the star are hampered, it does nonetheless appear that there may be good reasons for real differences to exist.

Along the sight line to HD 167756, which samples disk and low halo gas, GHRS 3.5 km s^{-1} resolution measurements reported by Savage et al. (1994) reveal the existence of two types of highly ionized gas. The first type is a hotter ($T \sim 2$–8×10^5 K) gas that is traced mainly by N V, and has N(C IV)/N(N V) ≈ 1.0. The second type is traced mainly by Si IV, has N(C IV)/N(Si IV) ≈ 3.5, and may arise in conductive interfaces between the warm and hot parcels of gas. C IV traces both types of gas and has more complex profiles then either N V or Si IV. A similar model could explain our measurements toward HD 116852 provided that the hotter phase containing N V is more confined to the Galactic plane than the Si IV-bearing phase.

Recent theoretical work on the ionization of gas in the Galactic halo by Shull & Slavin (1994) suggests that inhomogeneous ionization models of the ISM may account for differences in the scale heights and column density ratios of the high ions. In these models, isolated isobarically cooling supernova remnants provide the conditions necessary to produce hot gas near the Galactic plane, and turbulent mixing layers and superbubbles are responsible for hot gas at large distances from the plane. This picture is consistent with models of the evolution of supernova bubbles (Slavin & Cox 1992) and the prediction by Slavin & Cox (1993) that gas at large z-distances may require sources of ionization other than supernova bubbles to explain the observed high ion abundances. It is significant that the enhancement in the Si IV and C IV we see near -35 km s^{-1} has the lowest N(C IV)/N(Si IV) ratio of any velocity and is presumably associated with an outflow in the Norma-Centaurus spiral arm (see § 4). The effects of the changes in ionization for hybrid collisional ionization models are likely to be subtle, like those we see here, since the signatures of the different cooling hot gases in the high ion absorption profiles do not depend strongly on the initial conditions assumed for the gases. However, it would be difficult to produce the smoothly varying changes in N(C IV)/N(Si IV) by photoionization since such systematic changes require a remarkably smooth radiation field over extended paths (~5 kpc) through the disk and halo.

8. SUMMARY

We summarize the main results of our GHRS observations and analysis of the ionized interstellar medium toward HD 116852 as follows:

1. We have obtained GHRS G160M spectra of the interstellar Al III, Si IV, C IV, and N V doublet lines toward HD 116852 with resolutions of 11 to 18 km s^{-1} (FWHM) and S/N between 30 and 90. In these spectra we also detect low ion lines of interstellar C I, C I*, C I**, Si II, Mg II, Ge II, P II, S II, and Ni II.

2. We find that the stellar wind and photospheric lines in the ultraviolet spectrum of HD 116852 closely resemble those of the O9 III star ι Ori. This result is consistent with the optical MK classification of HD 116852 as a normal O9 III star with a spectroscopic distance of 4.8 kpc and a z-distance of -1.3 kpc.

3. We convert the complex Al III, Si IV, C IV, and N V absorption profiles into measures of apparent column density per unit velocity, $N_a(v)$. Comparisons of these profiles indicate that there is little ($<10\%$) unresolved saturated structure present in the observed profiles. From direct integration of the $N_a(v)$ profiles, we calculate total sight line column densities of $\log N = 13.26$, 13.54, 14.13, and 13.48 for Al III, Si IV, C IV, and N V, respectively.

4. A combination of gas scale height, velocity dispersion, and differential Galactic rotation effects governs the shapes of the observed absorption profiles. A simple computer model of the sight line gas distribution for the P II, Ge II, Al III, Si IV, C IV, and N V $N_a(v)$ profiles reveal that the velocity dispersions and scale heights of the gas increase as the ionization level of the gas increases.

5. The velocity dispersions we estimate from the positive velocity wings of the profiles, which are not influenced by Galactic rotation, range from $b_g < 15$ km s^{-1} for the low ions to $b_g = 19$, 23, 27, and 31 km s^{-1} for Al III, Si IV, C IV, and N V.

6. We obtain exponential scale heights of $H \leq 0.1$ kpc for the low ions, $H \approx 0.6$ to 0.7 kpc for Al III, and $H \geq 1$ kpc for Si IV, C IV, and N V.

7. Two types of component structure are present in the Al III profiles. A narrow, $b = 4.7$ km s^{-1}, component centered near -15 km s^{-1} contains approximately 25% of the Al III column density along the sight line and has $N(\text{Si IV})/N(\text{Al III}) \leq 1.3$. The narrow component probably arises within gas associated with the Sagittarius-Carina spiral arm link at a z-distance of about -0.5 kpc.

8. The second type of Al III structure is a broad, $b_g \approx 15$ to 20 km s^{-1}, distribution that tracks portions of the Si IV distribution. This distribution of components has a cloud-to-cloud dispersion and scale height that are consistent with those seen in other directions for the diffuse Hα emission in the Galaxy. Photoionization models cannot account for the observed Si IV and C IV absorption that appears to be associated with this gas.

9. The detection of N V indicates the presence of hot ($T \sim 10^5$ K), collisionally ionized gas along the sight line. We find $N(\text{C IV})/N(\text{N V}) \approx 4.3 \pm 0.8$ over the velocity range from -50 to $+30$ km s^{-1}. This ratio is consistent with a gas temperature of $T = 1\text{–}3 \times 10^5$ K.

10. We find $N(\text{C IV})/N(\text{Si IV}) = 3.8 \pm 0.6$ between -50 to $+30$ km s^{-1}. The ratio decreases from 4.5 near 0 km s^{-1} to 2.8 near -40 km s^{-1}. The decrease in this ratio can be explained by a model of the ionization structure of the ISM in which the nature of the ionization changes as a function of distance from the Galactic plane or by a two-phase hot gas model in which the relative contribution from each phase changes along the sight line. The enhancement near -35 km s^{-1} in both the Si IV and C IV profiles may be due to an outflow from the Norma spiral arm at a z-distance of about -1 kpc.

We thank the dedicated people involved with the *HST* and GHRS for making these observations possible. It is a pleasure to thank D. Massa for providing the initial version of the code used to construct the model column density profiles described in § 6 and R. Edgar and J. Bregman for useful suggestions concerning the content of the manuscript. We appreciate help from J. Cardelli in the preparation of the observing specifications associated with this program. Initial displays and reduction of the data were done at the Midwest Astronomical and Data Analysis Facility in Madison, Wisconsin. Secondary reduction, analysis, and computer modeling were performed at the Center for Space Research at the Massachusetts Institute of Technology. KRS acknowledges support from a Hubble Fellowship provided by NASA through grant number HF-1038.92A from the Space Telescope Science Institute, which is operated by AURA under NASA contract NAS5-26555. BDS recognizes support from NASA grant NAG5-1852.

REFERENCES

Abbott, D. C., Bohlin, R. C., & Savage, B. D. 1982, ApJS, 48, 369
Anders, E., & Grevesse, N. 1989, Geochim. Cosmochim. Acta, 53, 197
Balona, L. A. 1975, MmRAS, 78, 51
Berkuijsen, E. M., Haslam, C. G. T., & Salter, C. J. 1971, A&A, 14, 252
Bevington, P. R. 1969, Data Reduction and Error Analysis for the Physical Sciences (New York: McGraw-Hill)
Black, J. H., Dupree, A. K., Hartmann, L. W., & Raymond, J. C. 1980, Apl, 239, 502
Bok, B. J. 1971, in Highlights, in Astron., Vol. 2, ed. C. deJager (Washington: GPO), 63
Borkowski, K. J., Balbus, S. A., & Fristrom, C. C. 1990, ApJ, 355, 501
Bregman, J. N. 1980, ApJ, 236, 577
Bregman, J. N., & Harrington, P. J. 1986, ApJ, 309, 833
Burks, G. S., York, D. G., Blades, J. C., Bohlin, R. C., & Wamsteker, W. 1991, ApJ, 381, 55
Cardelli, J. A., Ebbets, D., & Savage, B. D. 1993, ApJ, 413, 401
Castor, J., McCray, R., & Weaver, R. 1975, ApJ, 200, L107
Chevalier, R. A., & Fransson, C. 1984, ApJ, 279, L43
Clements, D. P. 1985, ApJ, 295, 422
Colomb, F. R., Gil, M., & Morras, R. 1976, A&AS, 26, 195
Courtès, G. 1972, Vistas Astron., 14, 81
Courtès, G., Georgelin, Y. P., Georgelin, Y. M., & Monet, G. 1970, in IAU Symp. 38, The Spiral Structure of Our Galaxy, ed. W. Becker & G. Contopoulos (Dordrecht: Reidel), 209
Cowie, L. L., Taylor, W., & York, D. G. 1981, ApJ, 248, 528
Danly, L., Albert, C. E., & Kuntz, K. D. 1993, ApJ, 416, L29
Dettmar, R.-J. 1990, A&A, 232, L15
Diplas, A., & Savage, B. D. 1994, ApJ, in press
Diplas, A., & Sembach, K. R. 1994, in preparation
Duncan, D. K. 1992, Goddard High-Resolution Spectrograph Instrument Handbook, Version 3.0 (Baltimore: STScI)
Duncan, D. K., & Ebbets, D. C. 1990, Goddard High-Resolution Spectrograph Instrument Handbook, Version 2.1 (Baltimore: STScI)
Dupree, A. K., & Raymond, J. C. 1983, ApJ, 275, L71
Edgar, R. J., & Chevalier, R. A. 1986, ApJ, 310, L27
Edgar, R. J., & Savage, B. D. 1989, ApJ, 340, 762
Evans, I. N., & Dopita, M. A. 1985, ApJS, 58, 125
Feast, M. W., Thackeray, A. D., & Wesselink, A. J. 1963, MmRAS, 44, 134
Ferlet, R., Vidal-Madjar, A., & Gry, C. 1985, ApJ, 298, 838
Fransson, C., & Chevalier, R. A. 1985, 296, 35
Hartquist, T. W., Pettini, M., & Tallant, A. 1984, ApJ, 276, 519
Hartquist, T. W., Snijders, M. A. J., & West, K. A. 1983, MNRAS, 203, 1183
Heiles, C. 1982, ApJ, 262, 135
Hill, P. W., Kilkenny, D., & Van Breda, I. G. 1974, MNRAS, 168, 451
Hobbs, L. M., Welty, D. E., Morton, D. C., Spitzer, L., & York, D. G. 1993, ApJ, 411, 750
Hoffleit, D., & Jaschek, C. 1982, The Bright Star Catalogue, 4th ed. (New Haven: Yale Univ. Obs.)
Houck, J., & Bregman, J. N. 1990, ApJ, 352, 506
Howarth, I. D., & Prinja, R. K. 1989, ApJS, 69, 527

Iwan, D. 1980, ApJ, 239, 316

Jenkins, E. B. 1981, in The Universe at Ultraviolet Wavelengths, ed. R. D. Chapman (NASA CP-2171), 541

———. 1986, ApJ, 304, 739

———. 1987, in Interstellar Processes, ed. D. Hollenbach & H. A. Thronson (Dordrecht: Reidel), 533

Johnson, H. L. 1963, in Basic Astronomical Data, ed. K. A. Strand (Chicago: Univ. Chicago Press), 214

Kerr, F. J., Bowers, P. F., Jackson, P. D., & Kerr, M. 1986, A&AS, 66, 373

Koo, B. C., Heiles, C., & Reach, W. T. 1992, ApJ, 390, 108

Kulkarni, S. R., & Fich, M. 1985, ApJ, 289, 792

Lockman, F. J. 1984, ApJ, 283, 90

Lockman, F. J., & Gehman, C. S. 1991, ApJ, 382, 192

Marsáková, P. 1974, Ap&SS, 27, 3

Martos, M., & Cox, D. P. 1994, in preparation

McCammon, D. 1984, in IAU Colloq. 81, The Local Interstellar Medium, ed. Y. Kondo, F. C. Bruhweiler, & B. D. Savage (NASA CP-2345)

McCammon, D., Burrows, D. N., Sanders, W. T., & Kraushaar, W. L. 1983, ApJ, 269, 107

McKee, C., & Ostriker, J. 1977, ApJ, 218, 148

Mihalas, D., & Binney, J. 1981, Galactic Astronomy, 2d ed. (San Francisco: Freeman)

Moore, C. E. 1970, NSRDS-NBS 34

Morgan, W. W., Code, A. D., & Whitford, A. E. 1955, ApJS, 2, 41

Morton, D. C. 1991, ApJS, 77, 119

Norman, C., & Ikeuchi, S. 1989, ApJ, 345, 372

Nousek, J. A., Fried, P. M., Sanders, W. T., & Kraushaar, W. L. 1982, ApJ, 258, 83

Oort, J. 1977, ARA&A, 15, 295

Pettini, M., & West, K. A. 1982, ApJ, 260, 561

Press, W. H., Flannery, B. P., Teukolsky, S. A., & Vetterling, W. T. 1986, Numerical Recipes: The Art of Scientific Computing (Cambridge: Cambridge Univ. Press)

Prinja, R. K. 1990, MNRAS, 246, 392

Prinja, R. K., Barlow, M. J., & Howarth, I. D. 1990, ApJ, 361, 607

Reynolds, R. J. 1985, ApJ, 294, 256

———. 1993, in Back to the Galaxy, the Proc. of the 3rd Annual Astrophysics Conference in Maryland, ed. F. Verter (New York: AIP), 156

Rickard, J. J. 1974, A&A, 31, 47

Savage, B. D., Edgar, R. J., & Diplas, A. 1990, ApJ, 361, 107

Savage, B. D., Lu. L., Weymann, R., Morris, S., & Gilliland, R. 1993, ApJ, 404, 134

Savage, B. D., & Massa, D. 1987, ApJ, 314, 381

Savage, B. D., Massa, D., & Sembach, K. R. 1990, ApJ, 355, 114

Savage, B. D., & Mathis, J. 1979, ARA&A, 17, 73

Savage, B. D., & Sembach, K. R. 1991, ApJ, 379, 245

———. 1994, ApJ, in press

Savage, B. D., Sembach, K. R., & Cardelli, J. A. 1994, ApJ, 420, 183

Sembach, K. R., & Danks, A. 1994, A&A, in press

Sembach, K. R., Danks, A., & Savage, B. D. 1993, A&AS, 100, 107

Sembach, K. R., & Savage, B. D. 1992, ApJS, 83, 147

Sembach, K. R., Savage, B. D., & Jenkins, E. B. 1994, ApJ, 427, 585

Sembach, K. R., Savage, B. D., & Massa, D. 1991, ApJ, 372, 81

Shapiro, P. R., & Benjamin, R. A. 1993, in Star Forming Galaxies and Their Interstellar Media, ed. J. J. Franco (New York: Cambridge Univ. Press), 273

Shapiro, P. R., & Moore, R. T. 1976, ApJ, 207, 406

Shull, M. J., & Salvin, J. D. 1994, ApJ, in press

Slavin, J. D., & Cox, D. 1992, ApJ, 417, 187

———. 1993, ApJ, 392, 131

Sofia, U. J., & Cardelli, J., & Savage, B. D. 1994, ApJ, in press

Sokolowski, J. 1994, ApJ, submitted

Spitzer, L., Jr. 1978, Physical Processes in the Interstellar Medium (New York: Wiley)

Spitzer, L., & Fitzpatrick, E. 1992, ApJ, 391, L41

Steigman, G., Strittmater, P. A., & Williams, R. E. 1975, ApJ, 198, 575

Sutherland, R. S., & Dopita, M. A. 1993, ApJS, 88, 253

Wakker, B. P. 1991, in IAU Symp. 144, The Disk-Halo Interstellar Connection in Galaxies, ed. H. Bloemen (Dordrecht: Kluwer), 407

Walborn, N. R. 1973, AJ, 78, 1067

Walborn, N. R., Nichols-Bohlin, J., & Panek, R. J. 1985, *International Ultraviolet Explorer* Atlas of O-Type Spectra from 1200 to 1900 Å (NASA Ref. Pub. 1155)

Walborn, N. R., & Panek, R. J. 1984, ApJ, 280, L27

Weaver, R., McCray, R., Castor, J., Shapiro, P., & Moore, R. 1977, ApJ, 218, 377

York, D. G., Blades, J. C., Cowie, L. L., Morton, D. C., Songaila, A., & Wu, C. C. 1982, ApJ, 255, 467